INTERNATIONAL JOURNAL FOR NUMERICAL METHODS IN FLUIDS
Int. J. Numer. Meth. Fluids 2010; **62**:530–564
Published online 19 March 2009 in Wiley InterScience (www.interscience.wiley.com). DOI: 10.1002/fld.2029

Free surface Stokes flows obstructed by multiple obstacles

S. J. Baxter[1], H. Power[1,*,†], K. A. Cliffe[2] and S. Hibberd[2]

[1]*Fuels and Power Technology Research Division, Faculty of Engineering, The University of Nottingham, Nottingham NG7 2RD, U.K.*
[2]*School of Mathematical Sciences, The University of Nottingham, Nottingham NG7 2RD, U.K.*

SUMMARY

Gravity-driven Stokes flow down an inclined plane over and around multiple obstacles is considered. The flow problem is formulated in terms of a boundary integral equation and solved using the boundary element method. A Hermitian radial basis function (RBF) is used for the interpolation of the free surface, generation of the unit normal and curvature, and to prescribe the far-field conditions. For flow over an obstacle, hemispheres are taken. For flow around an obstacle, circular cylinders are modelled and the contact angle condition on the obstacle/free surface intersection specified using the RBF formulation. Explicit profiles are produced for flow over and around two obstacles placed in various locations relative to one another. Interaction due to two obstacles is given by comparisons made with the profiles for flow over and around individual obstacles. In general, when the obstacles are separated by a sufficiently large distance the flow profiles are identical to a single obstacle analysis. For flow over and around two obstacles in-line with the incident flow, effects of the governing parameters are examined, with variations in plane inclination angle, Bond number, obstacle size, and in the case of obstacles intersecting the free surface, static contact angle is considered. Finally flows over and around three obstacles are modelled. Copyright © 2009 John Wiley & Sons, Ltd.

Received 7 October 2008; Revised 15 January 2009; Accepted 6 February 2009

KEY WORDS: boundary integral equations; viscous flow; thin film; multiple obstacles; radial basis function interpolation; gravity-driven Stokes flow

1. INTRODUCTION

Stokes equations can be used to model the flow of a thin film down an inclined plane. For flow over or around an obstacle the resulting flow profiles are of practical interest, for instance in spin coating as considered by Stillwagon and Larson [1] and Peurrung and Graves [2] among

*Correspondence to: H. Power, School of Mechanical, Materials and Manufacturing Engineering, The University of Nottingham, Nottingham NG7 2RD, U.K.
†E-mail: henry.power@nottingham.ac.uk

Contract/grant sponsor: EPSRC and Rolls-Royce plc, Aerospace Group

others. A more complex problem is the fluid/obstacle interaction of multiple obstacles where the disturbance profiles local to each obstacle can interact, resulting in significant differences compared with the flow profile generated in the single obstacle case. An example is in the lubrication process of a bearing chamber of an aero-engine, with the free surface flow interacting with various configurations of chamber supports and intrusions.

Film flow over two-dimensional obstructions can be solved by an extensive range of numerical methods, and an overview of many key papers is available in Blyth and Pozrikidis [3]. Owing to the added complexity in solving the full three-dimensional flow problem, restricted approaches are available for analysis, with a lubrication approximation the most popular approach. However, due to the additional simplification, problems arise with validity of this assumption where the flow profiles become steep. This problem is not present with a Stokes flow analysis, but such analysis is currently less widely available.

Hayes *et al.* [4] and Gaskell *et al.* [5] analysed a gravity-driven thin film over topographies on an inclined plane, based on a lubrication approximation. Hayes *et al.* [4] solved the flow problem via formation of a Green's function with a solution produced for flow over a small steep obstruction. Gaskell *et al.* [5] analysed the accuracy of modelling flow over a steep sided topography using lubrication theory. Comparisons were made with solutions to the full Navier–Stokes equations using a finite element method, with a good agreement between the two methods reported. Lee *et al.* [6] modelled the thin film flow over both single and multiple obstructions using the lubrication approximation. Profiles over a single square, diamond, and circular trench were considered. Flow over complex multiple obstacle configurations consisting of a central diamond trench with two circular trenches downstream and two circular struts upstream was also considered.

Sellier [7] also used lubrication theory to consider flow around a circular cylinder. However, the solutions fail to satisfy no slip at the cylinder wall and the limitation of the lubrication approximation with steep profiles remains.

The solution of three-dimensional, free surface Stokes flows over a single obstacle via the formulation of the boundary integral equations (BIEs) has been conducted in fewer papers. Early work produced by Pozrikidis and Thoroddsen [8] solved the free surface via the integral equations and modelled the obstruction to be asymptotically small when compared with the film depth. This approach was later refined by Blyth and Pozrikidis [3] and adopted for the most recent work by Baxter *et al.* [9]. Blyth and Pozrikidis [3] implement a modified version of [8] incorporating the BIEs for solution of the obstacle surface and corrects a small error in the earlier formulation. Results for flow over a hemispherical obstacle produce characteristic results of a large upstream peak decaying in a 'horseshoe'-like fashion, with a shallow trough present for a long distance downstream. Profiles are qualitatively comparable to an asymptotic obstacle analysis, although the integral model of the obstacle failed to produce solutions for sufficiently small obstacles to confirm consistency of solutions. Both the work of Pozrikidis and Thoroddsen [8] and Blyth and Pozrikidis [3] use a linearization of the free surface deflection, and as such the accuracy of the model for large free surface deformations for flow over large obstacles is limited.

Recent work by Baxter *et al.* [9], extends the formulations of [3, 8], and removes the linearized free surface condition through implementation of a Hermitian radial basis function (RBF) for evaluation of the free surface quantities. Results of [3, 8] have been reproduced, with consistency found between the asymptotic and full obstacle analysis. Removal of the free surface linearization allowed flow over hemispheres to be analysed that approach the free surface and in addition, by implementation of a contact line condition within the RBF the flow around a circular cylinder

DOI: 10.1002/fld

evaluated. Baxter *et al.* [9] also demonstrated the possibility of multiple solutions, where a flow profile may exist both over and around a circular cylinder for the same flow parameters.

A numerical technique is implemented that extends the boundary integral formulation first outlined in Blyth and Pozrikidis [3] and developed by Baxter *et al.* [9], allowing the analysis of a Stokes flow down an inclined plane over and around multiple obstacles. As in [9], the free surface is interpolated by a Hermitian RBF used for calculation of free surface quantities. A range of configurations for both two and three hemispheres fully contained within the film and two or three circular cylinders that penetrate the free surface are analysed. In both cases, the corresponding profiles for a single obstacle are shown to be reproduced when the separation distances between obstructions is sufficiently large.

2. PROBLEM FORMULATION

A two-dimensional illustration of a typical film flow around N obstacles intersecting the free surface is shown in Figure 1. The upstream uniform film has an undisturbed thickness H, and the plane S_w is inclined at an angle α. The disturbed free surface is denoted S_f and the undisturbed free surface S_π. The obstacle/fluid boundary is denoted S_p^l, with the surface outside of the fluid given by $\tilde{S}_f^l$, for $l=1,\ldots,N$. The disturbance of the free surface from S_π is given by h, and the outward unit normal is denoted $\mathbf{n}$. The cartesian co-ordinate axis is aligned so that x_1, x_2 span the plane S_π, with x_1 in the direction of the far-field flow, and x_3 perpendicular to S_π.

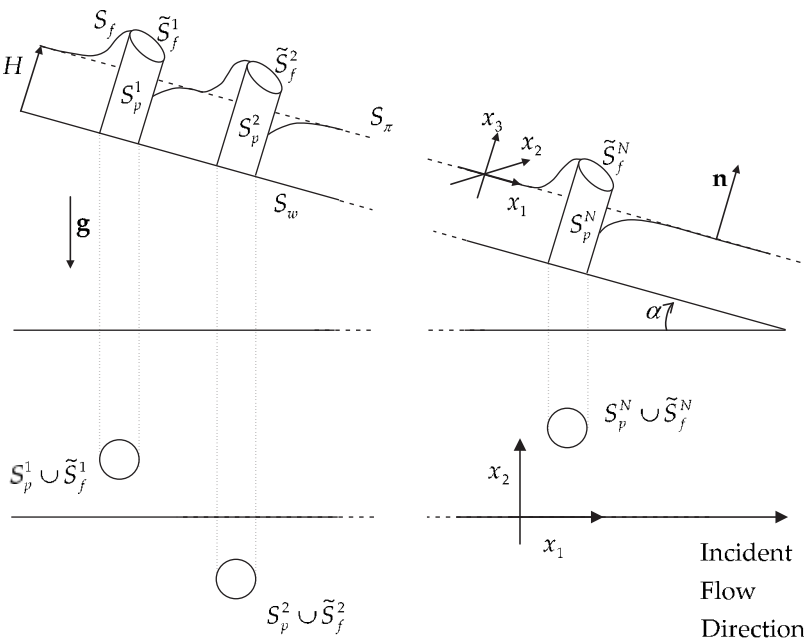

Figure 1. Schematic of a typical flow profile around N obstacles; cross-section and plan view.

DOI: 10.1002/fld

Physical variables are taken as non-dimensionalized based around the Nusselt solution for Stokes flow down an inclined plane in the absence of any obstacles. The undisturbed film height, H, is chosen as the reference length, the velocity at the undisturbed film surface, $U_s = H^2 \rho g \sin\alpha / 2\mu$, is used as the reference velocity, and a viscous scaling, $\mu U_s / H$, used as the reference stress. The Bond number is defined as

$$Bo = \frac{\rho g H^2 \sin\alpha}{\gamma} \tag{1}$$

where g is acceleration due to gravity, ρ is the fluid density, and γ is the surface tension.

Steady, incompressible Stokes flow down an inclined plane is governed by

$$\frac{\partial u_i}{\partial x_i} = 0 \tag{2}$$

$$-\frac{\partial p}{\partial x_i} + \frac{\partial G}{\partial x_i} + \frac{\partial^2 u_i}{\partial x_j^2} = 0 \tag{3}$$

where the gravitational component G is defined by,

$$G = -2(x_3 \cot\alpha - x_1) \tag{4}$$

The far-field boundary conditions require the velocity and pressure returning to the associated Nusselt solution for flow in the absence of obstacles, and the free surface disturbance decaying to zero, i.e.

$$\left.\begin{aligned} u_i &\to u_i^{\infty} \\ p &\to p^{\infty} \\ h &\to 0 \\ \frac{\partial h}{\partial x_1} &\to 0 \\ \frac{\partial h}{\partial x_2} &\to 0 \end{aligned}\right\} \quad \text{as } \mathbf{x} \to \pm\infty \tag{5}$$

The flow problem also requires no slip on the fluid/obstacle boundary and plane together with a kinematic and dynamic condition imposed on the free surface. These boundary conditions are given in expressions (6)–(8), where t is the time, f_i the boundary traction, κ the curvature of the free surface, and σ_{ij} is the stress tensor

$$u_i = 0, \quad \mathbf{x} \in S_w \cup S_p^1 \cup \cdots \cup S_p^N \tag{6}$$

$$\frac{\partial x_i}{\partial t} n_i = u_j n_j, \quad \mathbf{x} \in S_f \tag{7}$$

$$f_i = \sigma_{ij} n_j = -\frac{4}{Bo} \kappa n_i, \quad \mathbf{x} \in S_f \tag{8}$$

DOI: 10.1002/fld

Expressions for the curvature and stress tensor are given in (9) and (10), where n_i is the outward unit normal of the free surface

$$\kappa = \frac{1}{2}\frac{\partial n_i}{\partial x_i} \tag{9}$$

$$\sigma_{ij} = -p\delta_{ij} + \left(\frac{\partial u_i}{\partial x_j} + \frac{\partial u_j}{\partial x_i}\right) \tag{10}$$

Expressed in terms of the deflection height h of the free surface, the outward unit normal is

$$\mathbf{n} = \frac{1}{\sqrt{1+\left(\dfrac{\partial h}{\partial x_1}\right)^2+\left(\dfrac{\partial h}{\partial x_2}\right)^2}}\left(-\frac{\partial h}{\partial x_1}, -\frac{\partial h}{\partial x_2}, 1\right) \tag{11}$$

and the curvature is given by

$$\kappa = -\frac{1}{2}\left(1+\left(\frac{\partial h}{\partial x_1}\right)^2+\left(\frac{\partial h}{\partial x_2}\right)^2\right)^{-3/2} \times\left[\frac{\partial^2 h}{\partial x_1^2}\left(1+\left(\frac{\partial h}{\partial x_2}\right)^2\right)+\frac{\partial^2 h}{\partial x_2^2}\left(1+\left(\frac{\partial h}{\partial x_1}\right)^2\right)-2\frac{\partial h}{\partial x_1 \partial x_2}\frac{\partial h}{\partial x_1}\frac{\partial h}{\partial x_2}\right] \tag{12}$$

For obstacles perpendicular to the plane that penetrates the free surface, a static contact line condition is applied at the obstacle/free surface interface, and given by,

$$\frac{\partial h}{\partial x_i} n_i = \tan\left(\frac{\pi}{2} - \theta\right) \tag{13}$$

where θ is the contact angle between the liquid and the solid surface.

The governing equations and boundary conditions (2)–(13) can be solved for the flow to evaluate the effect of obstacles on the free surface profile. However, the computational problem can be simplified by reformulating the problem in terms of an undisturbed or asymptotic regime of a flow with no obstacles, and a disturbance regime. Variables associated with the undisturbed regime are denoted by a superscript ∞, and variables associated with the disturbance regime are denoted by a superscript δ.

Undisturbed regime: Steady Stokes flow in the absence of obstacles is governed by

$$\frac{\partial u_i^\infty}{\partial x_i} = 0 \tag{14}$$

$$-\frac{\partial p^\infty}{\partial x_i} + \frac{\partial G}{\partial x_i} + \frac{\partial^2 u_i^\infty}{\partial x_j^2} = 0 \tag{15}$$

DOI: 10.1002/fld

The boundary conditions for the undisturbed flow regime include no slip on the inclined plane, and a zero boundary traction at the free surface. Thus,

$$u_i^\infty = 0, \quad \mathbf{x} \in S_w \tag{16}$$

$$f_i^\infty = 0, \quad \mathbf{x} \in S_\pi \tag{17}$$

and solutions for u_i^∞, p^∞, and $f_i^\infty = \sigma_{ij}(p^\infty, u_k^\infty)n_j$ are

$$p^\infty = -2x_3 \cot\alpha \tag{18}$$

$$u_i^\infty = (1 - x_3^2)\delta_{i1} \tag{19}$$

$$f_i^\infty = 2x_3(n_i \cot\alpha - n_3\delta_{i1} - n_1\delta_{i3}) \tag{20}$$

These solutions are used to determine the conditions for the disturbance flow caused by the obstacles.

Disturbance regime: The velocities and pressures associated with the disturbance regime are defined by

$$u_i = u_i^\delta + u_i^\infty \tag{21}$$

$$p = p^\delta + p^\infty \tag{22}$$

and the governing equations for the disturbance quantities are

$$\frac{\partial u_i^\delta}{\partial x_i} = 0 \tag{23}$$

$$-\frac{\partial p^\delta}{\partial x_i} + \frac{\partial^2 u_i^\delta}{\partial x_j^2} = 0 \tag{24}$$

found by comparing (2) and (3) with (14) and (15).

The flow returns to undisturbed values in the far field (5), with the disturbance far-field conditions given by

$$\left.\begin{aligned} u_i^\delta &\to 0 \\ p^\delta &\to 0 \end{aligned}\right\} \quad \text{as } \mathbf{x} \to \pm\infty \tag{25}$$

The no-slip conditions (6) and (16) require the disturbance velocities to satisfy,

$$u_i^\delta = 0, \quad \mathbf{x} \in S_w \tag{26}$$

$$u_i^\delta = -u_i^\infty, \quad \mathbf{x} \in S_p^1 \cup \cdots \cup S_p^N \tag{27}$$

Finally the disturbance boundary traction can be found by comparing (8) and (20) to yield

$$f_i^\delta = -\frac{4}{Bo}\kappa n_i - 2x_3(n_i \cot\alpha - n_3\delta_{i1} - n_1\delta_{i3}) \tag{28}$$

on the free surface S_f.

Boundary integral formulation: The Stokes flow equations for the disturbance regime can be represented exactly by the BIE given as (29) over the fluid domain. It is noted that the edges of

DOI: 10.1002/fld

the domain are omitted from the integrals due to u_i^δ and f_i^δ decaying to zero in the far field. In addition, the wall S_w is removed from the integrals by use of Lorentz–Blake Green's functions, satisfying $G_{ij}^*(\mathbf{x},\mathbf{x}_0)=0$ on the wall, and the no-slip condition (26). The form of Lorentz–Blake Green's functions is given in the Appendix and the disturbance BIE is

$$c_{ij}(\mathbf{x}_0)u_i^\delta(\mathbf{x}_0)=\frac{1}{8\pi}\int_{S_f\cup S_p^1\cup\cdots\cup S_p^N} G_{ij}^*(\mathbf{x},\mathbf{x}_0)\,f_i^\delta(\mathbf{x})\mathrm{d}S(\mathbf{x}) \\ -\frac{1}{8\pi}\int_{S_f\cup S_p^1\cup\cdots\cup S_p^N} u_i^\delta(\mathbf{x})T_{ijk}^*(\mathbf{x},\mathbf{x}_0)n_k(\mathbf{x})\mathrm{d}S(\mathbf{x}) \tag{29}$$

where $\mathbf{x}$ is the field point and $\mathbf{x}_0$ any collocation point. The coefficient $c_{ij}(\mathbf{x}_0)$ is given piecewise by

$$c_{ij}(\mathbf{x}_0)=\begin{cases}0, & \mathbf{x}_0 \text{ outside the domain}\\ \frac{1}{2}\delta_{ij}, & \mathbf{x}_0 \text{ on the boundary of the domain}\\ \delta_{ij}, & \mathbf{x}_0 \text{ within the domain}\end{cases} \tag{30}$$

For the N closed domains $S_p^l\cup\tilde{S}_f^l$, $l=1,\ldots,N$, the undisturbed quantities u_i^∞ and $p^\infty-G$ satisfy the N BIEs

$$c_{ij}(\mathbf{x}_0)u_i^\infty(\mathbf{x}_0)=-\frac{1}{8\pi}\int_{S_p^l\cup\tilde{S}_f^l} G_{ij}^*(\mathbf{x},\mathbf{x}_0)(f_i^\infty(\mathbf{x})+Gn_i(\mathbf{x}))\mathrm{d}S(\mathbf{x}) \\ +\frac{1}{8\pi}\int_{S_p^l\cup\tilde{S}_f^l} u_i^\infty(\mathbf{x})T_{ijk}^*(\mathbf{x},\mathbf{x}_0)n_k(\mathbf{x})\mathrm{d}S(\mathbf{x}) \tag{31}$$

for $l=1,\ldots,N$. It is noted that for both BIEs (29) and (31), the unit normal is taken outward to the fluid domain, and is thus inward to the integration domain in (31), explaining the change in sign for the single and double layer potential.

When $\mathbf{x}_0$ lies outside of all obstacle domains and their boundaries, use of (30) shows the BIE (31) to reduce to

$$\frac{1}{8\pi}\int_{S_p^l\cup\tilde{S}_f^l} G_{ij}^*(\mathbf{x},\mathbf{x}_0)(f_i^\infty(\mathbf{x})+Gn_i(\mathbf{x}))\mathrm{d}S(\mathbf{x})=\frac{1}{8\pi}\int_{S_p^l\cup\tilde{S}_f^l} u_i^\infty(\mathbf{x})T_{ijk}^*(\mathbf{x},\mathbf{x}_0)n_k(\mathbf{x})\mathrm{d}S(\mathbf{x}) \tag{32}$$

for $l=1,\ldots,N$. Using the disturbance BIE (29) applied on $\mathbf{x}_0\in S_f$, and combining with BIEs (32) along with no-slip condition (27) yields

$$\frac{1}{2}u_j^\delta(\mathbf{x}_0)+\frac{1}{8\pi}\int_{S_f} u_i^\delta(\mathbf{x})T_{ijk}^*(\mathbf{x},\mathbf{x}_0)n_k(\mathbf{x})\mathrm{d}S(\mathbf{x}) \\ =\frac{1}{8\pi}\int_{S_p^1\cup\cdots\cup S_p^N} G_{ij}^*(\mathbf{x},\mathbf{x}_0)\,\tilde{f}_i(\mathbf{x})\mathrm{d}S(\mathbf{x})+\frac{1}{8\pi}\int_{\tilde{S}_f^1\cup\cdots\cup\tilde{S}_f^N} G_{ij}^*(\mathbf{x},\mathbf{x}_0)(f_i^\infty(\mathbf{x})+Gn_i(\mathbf{x}))\mathrm{d}S(\mathbf{x}) \\ -\frac{1}{8\pi}\int_{\tilde{S}_f^1\cup\cdots\cup\tilde{S}_f^N} u_i^\infty(\mathbf{x})T_{ijk}^*(\mathbf{x},\mathbf{x}_0)n_k(\mathbf{x})\mathrm{d}S(\mathbf{x})+\frac{1}{8\pi}\int_{S_f} G_{ij}^*(\mathbf{x},\mathbf{x}_0)\,f_i^\delta(\mathbf{x})\mathrm{d}S(\mathbf{x}),\quad \mathbf{x}_0\in S_f \tag{33}$$

where $\tilde{f}_i(\mathbf{x})=f_i(\mathbf{x})+Gn_i(\mathbf{x})$. The BIE (33) is defined for collocation points over the free surface.

DOI: 10.1002/fld

Applying BIE (31) at $\mathbf{x}_0 \in S_p^k$, a specific obstacle yields two possibilities; BIE (32) is applicable for $l = 1, \ldots, k-1, k+1, \ldots, N$, and

$$\frac{1}{2}u_j^\infty(\mathbf{x}_0) = -\frac{1}{8\pi}\int_{S_p^l \cup \tilde{S}_f^l} G_{ij}^*(\mathbf{x}, \mathbf{x}_0)(f_i^\infty(\mathbf{x}) + Gn_i(\mathbf{x}))\mathrm{d}S(\mathbf{x}) + \frac{1}{8\pi}\int_{S_p^l \cup \tilde{S}_f^l} u_i^\infty(\mathbf{x}) T_{ijk}^*(\mathbf{x}, \mathbf{x}_0) n_k(\mathbf{x})\mathrm{d}S(\mathbf{x}) \tag{34}$$

is used for $l = k$. BIE (29) is applied on the obstacle S_p^k, with the no-slip condition (27) also imposed to obtain

$$-\frac{1}{2}u_j^\infty(\mathbf{x}_0) = \frac{1}{8\pi}\int_{S_f} G_{ij}^*(\mathbf{x}, \mathbf{x}_0) f_i^\delta(\mathbf{x})\mathrm{d}S(\mathbf{x}) - \frac{1}{8\pi}\int_{S_f} u_i^\delta(\mathbf{x}) T_{ijk}^*(\mathbf{x}, \mathbf{x}_0) n_k(\mathbf{x})\mathrm{d}S(\mathbf{x}) + \frac{1}{8\pi}\int_{S_p^1 \cup \cdots \cup S_p^N} G_{ij}^*(\mathbf{x}, \mathbf{x}_0) f_i^\delta(\mathbf{x})\mathrm{d}S(\mathbf{x}) + \frac{1}{8\pi}\int_{S_p^1 \cup \cdots \cup S_p^N} u_i^\infty(\mathbf{x}) T_{ijk}^*(\mathbf{x}, \mathbf{x}_0) n_k(\mathbf{x})\mathrm{d}S(\mathbf{x}) \tag{35}$$

Combining BIE (35) with (32) and (34) yields a BIE for collocation over the obstacle S_p^k

$$\begin{aligned}
&\frac{1}{8\pi}\int_{S_p^k} G_{ij}^*(\mathbf{x}, \mathbf{x}_0)\tilde{f}_i(\mathbf{x})\mathrm{d}S(\mathbf{x}) + \frac{1}{8\pi}\int_{S_p^1 \cup \cdots \cup S_p^{k-1} \cup S_p^{k+1} \cup \cdots \cup S_p^N} G_{ij}^*(\mathbf{x}, \mathbf{x}_0)\tilde{f}_i(\mathbf{x})\mathrm{d}S(\mathbf{x}) \\
&= -u_j^\infty(\mathbf{x}_0) - \frac{1}{8\pi}\int_{S_f} G_{ij}^*(\mathbf{x}, \mathbf{x}_0) f_i^\delta(\mathbf{x})\mathrm{d}S(\mathbf{x}) + \frac{1}{8\pi}\int_{S_f} u_i^\delta(\mathbf{x}) T_{ijk}^*(\mathbf{x}, \mathbf{x}_0) n_k(\mathbf{x})\mathrm{d}S(\mathbf{x}) \\
&\quad - \frac{1}{8\pi}\int_{\tilde{S}_f^1 \cup \cdots \cup \tilde{S}_f^N} G_{ij}^*(\mathbf{x}, \mathbf{x}_0)(f_i^\infty(\mathbf{x}) + Gn_i(\mathbf{x}))\mathrm{d}S(\mathbf{x}) \\
&\quad + \frac{1}{8\pi}\int_{\tilde{S}_f^1 \cup \cdots \cup \tilde{S}_f^N} u_i^\infty(\mathbf{x}) T_{ijk}^*(\mathbf{x}, \mathbf{x}_0) n_k(\mathbf{x})\mathrm{d}S(\mathbf{x}), \quad \mathbf{x}_0 \in S_p^k
\end{aligned} \tag{36}$$

with this BIE holding for each $S_p^k, k = 1, \ldots, N$.

For the cases where flow is purely over obstacles fully contained within the fluid, BIEs (33) and (36) are reduced by omitting the integrals over $\tilde{S}_f^l$ for $l = 1, \ldots, N$.

2.1. Numerical schemes

Following the numerical scheme of Baxter *et al.* [9] in the present case of multiple obstacles, the unknown integral densities u_i^δ on S_f, and $\tilde{f}_i$ on $S_p^1 \cup \cdots \cup S_p^N$ are obtained by the following procedure:

1. Initially at the free surface elements plan view mid-points $\mathbf{x}^m = (x_1^m, x_2^m)$, a film profile is defined by heights h with corresponding disturbance velocities u_i^δ.

DOI: 10.1002/fld

2. A RBF is applied to the free surface S_f to find:
   (a) the heights at the nodal points of each free surface element $\mathbf{x}^n = (x_1^n, x_2^n)$,
   (b) the outward unit normal of the free surface at the element mid-points, $\mathbf{x}^m$,
   (c) the curvature of the free surface at the element mid-points, $\mathbf{x}^m$.
3. The disturbance boundary traction at the free surface element mid-points $\mathbf{x}^m$ is calculated by use of the dynamic condition (28).
4. The obstacle BIEs (36) are collocated over all obstacles/fluid surfaces S_p^k, $k = 1, \ldots, N$, for tractions $\tilde{f}_i$. Solutions are obtained by using the boundary element method (BEM), details of which are given later.
5. The free surface BIE (33) is collocated over S_f for the free surface disturbance velocities at each element mid-points. It is noted that the height of the element mid-points is approximated within this BEM formulation by the average of the nodal point heights.
6. The kinematic condition (7) is applied with the current values of h and the calculated values of u_i^δ at element mid-points $\mathbf{x}^m$, to find an updated set of h defining the free surface.
7. The process is repeated from step 2 using the new film profile.

It is emphasized that the only place that the free surface height is approximated is for collocation over the free surface within the BEM. In all other calculations, the height at any mid element location is associated with the interpolated surface. This limitation is caused by implementing flat triangular elements within the BIE.

The numerical schemes required to solve the problem are now discussed. This includes the various locations of the far-field conditions and obstacles, form for the meshes used for the free surface and obstacle, implementation of the BEM for solution of the BIEs (33) and (36), and the implementation of the RBF to evaluate the free surface position and various quantities such as curvature and unit normal.

2.1.1. Flow configuration and surface discretizations. For flow over or around a single obstacle located at (0,0), appropriate far-field conditions, denoted by $x_{1_{\min}} \leqslant x_1 \leqslant x_{1_{\max}}$ and $x_{2_{\min}} \leqslant x_2 \leqslant x_{2_{\max}}$ were found in Baxter *et al.* [9]. For multiple obstacles, with centres separated by $(x_{1_{\text{sep}}}, x_{2_{\text{sep}}})$, the far-field conditions can be extended to $x_{1_{\min}} - x_{1_{\text{sep}}}/2 \leqslant x_1 \leqslant x_{1_{\max}} + x_{1_{\text{sep}}}/2$ and $x_{2_{\min}} - x_{2_{\text{sep}}}/2 \leqslant x_2 \leqslant x_{2_{\max}} + x_{2_{\text{sep}}}/2$.

The obstacle/fluid boundaries, free surface, and virtual obstacle tops (for the case of flow around cylinders) all require discretization. Hemispherical obstacles are used for 'flow over' configurations and circular cylinders modelled when intersection of the free surface occurs. Obstacle meshes (including their tops where necessary) are generated as in [9] and details are omitted here. Free surface meshes are modified from the earlier work [9] and discussed briefly below.

For flow over single/multiple hemispheres, an inner refined mesh is defined that extends just beyond the edges of the region covered by all obstacle centres, $-x_{1_{\text{sep}}}/2 \leqslant x_1 \leqslant x_{1_{\text{sep}}}/2$, $-x_{2_{\text{sep}}}/2 \leqslant x_2 \leqslant x_{2_{\text{sep}}}/2$. Free surface meshes are formed by first creating a mesh of quadrilateral basis elements (usually square for the inner and outer regions) and then subdividing these into four by connecting diagonally opposite vertices. Inner mesh basis elements are sized as 0.5×0.5 with outer basis elements sized as 1.0×1.0. These were found to give sufficient accuracy for all meshes. Analysis of the inner mesh region is conducted to minimize the mesh size while limiting any long thin elements that may be formed. Figure 2 illustrates a typical free surface mesh for flow over an array of hemispheres contained within $-2 \leqslant x_1 \leqslant 2$ and $-2 \leqslant x_2 \leqslant 2$. The transition

DOI: 10.1002/fld

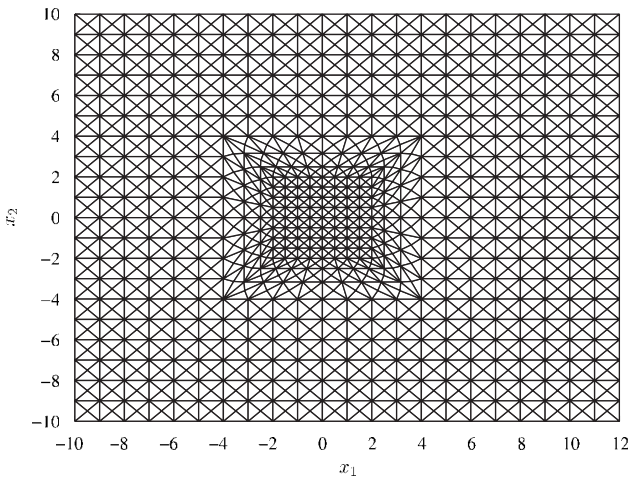

Figure 2. Typical free surface mesh for flow over an array of hemispheres.

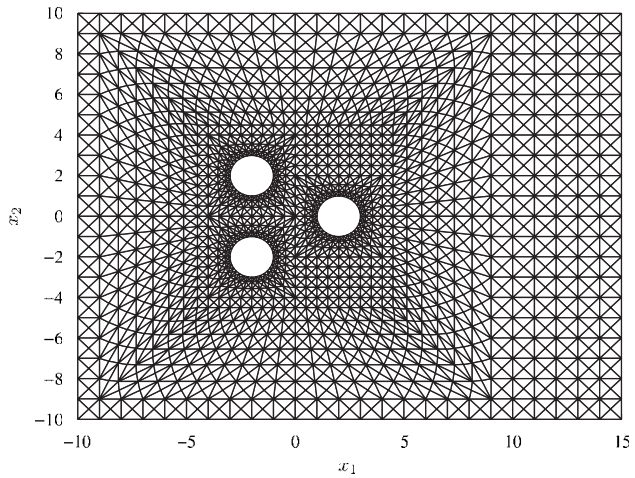

Figure 3. Typical free surface mesh for flow around an array of three circular cylinders.

region between the inner and outer uniform meshes is conducted by similar means as the cylinder to outer mesh technique used in Baxter *et al.* [9].

Free surface meshes for flow around multiple cylinders use alternative methods depending on the separation distance between the cylinders. If the cylinders are sufficiently far apart the mesh is formed by identical means to Baxter *et al.* [9]. If the transition meshes from each cylinder to the outer mesh overlap, then modification of this technique is required. An intermediate mesh with smaller element size than the outer mesh is defined. The cylinders are fitted to the intermediate mesh, and the intermediate mesh is then extended to the outer mesh. Figure 3 indicates a typical free surface mesh for this later case where flow is around three cylinders close to one another.

DOI: 10.1002/fld

2.1.2. The boundary element method. The BEM is used to solve the BIEs within the problem formulation. The discretization of the surfaces used was described above, and in addition, the BEM requires the type of elements used in the discretization and appropriate integration techniques to be defined.

The BEM implements linear geometric triangular elements throughout with a constant functional value associated with the mid-point of the element. Integration is conducted by identical means to Baxter *et al.* [9], with standard numerical integration techniques used throughout except for elements with a singular velocity Green's function, where polar integration was employed.

Near-point singularities cause conventional BIE formulations to fail when excessively thin regions of the computational domain are present. Krishnasamy *et al.* [10] summarized two classes of failure: the first is that the BIE coefficient matrix becomes increasingly ill-conditioned as the thin region becomes more extensive; and the second is that each integral within the thin region becomes nearly singular, causing difficulties in its accurate evaluation by standard numerical techniques. The authors also noted that improving the numerical schemes only results in limited success, with the ill-conditioning eventually becoming too severe.

Several techniques are reported in the literature to deal with near-singular integration. They include element subdivision [11], adaptive Gaussian integration [12], variable transformation techniques and semi-analytical integration based on series expansions and removal of singularities [13], besides others. In this work, the effects of ill-conditioning are not considered and improvements in the numerical integration scheme follow a method similar to that outlined in Cutanda *et al.* [14], and consists of a combination of the adaptive Gaussian integration algorithm and the element subdivision approach. Cutanda's *et al.* [14] approach of dealing with near-singular integrals was chosen due to its simplicity of formulation, although it is known that some of the other approaches, such as variable transformation and semi-analytical integration, are numerically more efficient.

The near-point singularity analysis was conducted identically to Baxter *et al.* [9], with the same bounding points used for determining the numerical integration regime, and displayed in Table I. This involved a 3-point Gaussian quadrature scheme used for singularity to element distance d greater than d_1, a 6-point scheme for $d_2 < d \leqslant d_1$, a 9-point scheme for $d_3 < d \leqslant d_2$, and a 13-point scheme for $d_4 < d \leqslant d_3$. If $d \leqslant d_4$ then the triangular element is divided into four smaller triangular elements each integrated with 13-point Gaussian quadrature. This subdivision method is repeated down to a possible five successive subdivisions. The added benefit of this method is to only increase the integration requirements in regions that are nearly singular, and as a result the effects on computation time were not too prohibitive.

2.1.3. Radial basis functions. A global Hermitian RBF interpolation of the fluid free surface is implemented. The RBF allows incorporation of the far-field derivative conditions and also the contact line condition for each obstacle that penetrates the free surface. The free surface height is given by $h(x_1, x_2)$, and for N distinct points, specific values h^i are known. Interpolation of the surface using a thin plate spline RBF of the form $\psi = r^4 \log r$ is used and chosen to remove

Table I. Bounding values for the near-point singularity analysis.

Bounding point	d_1	d_2	d_3	d_4	d_5	d_6	d_7	d_8
Bounding value	0.6	0.45	0.3	0.2	0.15	0.1	0.0316	0.01

DOI: 10.1002/fld

singularities of ψ at $r=0$ for up to and including the second derivative as required for evaluation of the free surface curvature (12). However, from La Rocca *et al.* [15] the exponent of r in ψ should be as small as possible to minimize ill-conditioning effects found in the interpolation matrix. In addition, to guarantee invertibility when using a thin plate spline, an additional polynomial of order 2 is used. The addition of the polynomial is required since it is known that the generalized thin plate spline of power $(2m-2)$ is a conditionally positive-definite function of order m, which requires the addition of a polynomial term of order $m-1$, together with a homogeneous constraint condition, in order to obtain an invertible interpolation matrix (for more details, see, Golberg and Chen [16]). In our case, we are using $m=3$ requiring a second-order polynomial.

The RBF can be used to additionally constrain the free surface gradient for the n far-field points and the n^{cl} contact line points. Surface displacements are then represented by

$$h(x_1^i, x_2^i) = \sum_{j=1}^{N} \lambda_j \psi + \sum_{j=1}^{n} \lambda_{N+j} \frac{\partial \psi}{\partial \xi_1} + \sum_{j=1}^{n} \lambda_{N+n+j} \frac{\partial \psi}{\partial \xi_2} + \sum_{j=1}^{n^{\mathrm{cl}}} \lambda_{N+n+n+j} \left(n_{\xi_1} \frac{\partial \psi}{\partial \xi_1} + n_{\xi_2} \frac{\partial \psi}{\partial \xi_2} \right) + P_2(\mathbf{x}) \tag{37}$$

with $\psi = \psi(\|\mathbf{x}^i - \boldsymbol{\xi}^j\|)$ as the thin plate spline interpolant function. The obstacles unit normal at the point $\boldsymbol{\xi}^j$ is given by $n_{\boldsymbol{\xi}^j} = (n_{\xi_1^j}, n_{\xi_2^j})$ and the polynomial term is given by

$$P_2(\mathbf{x}^i) = \lambda_{N+2n+n^{\mathrm{cl}}+1}(x_1^i)^2 + \lambda_{N+2n+n^{\mathrm{cl}}+2} x_1^i x_2^i + \lambda_{N+2n+n^{\mathrm{cl}}+3}(x_2^i)^2 + \lambda_{N+2n+n^{\mathrm{cl}}+4} x_1^i + \lambda_{N+2n+n^{\mathrm{cl}}+5} x_2^i + \lambda_{N+2n+n^{\mathrm{cl}}+6} \tag{38}$$

Values for the derivatives $\partial h/\partial x_1$ and $\partial h/\partial x_2$ are required and given by

$$\frac{\partial h}{\partial x_1} = \sum_{j=1}^{N} \lambda_j \frac{\partial \psi}{\partial x_1} + \sum_{j=1}^{n} \lambda_{N+j} \frac{\partial^2 \psi}{\partial \xi_1 \partial x_1} + \sum_{j=1}^{n} \lambda_{N+n+j} \frac{\partial^2 \psi}{\partial \xi_2 \partial x_1} + \sum_{j=1}^{n^{\mathrm{cl}}} \lambda_{N+n+n+j} \left(n_{\xi_1} \frac{\partial^2 \psi}{\partial \xi_1 \partial x_1} + n_{\xi_2} \frac{\partial^2 \psi}{\partial \xi_2 \partial x_1} \right) + \frac{\partial P_2(\mathbf{x})}{\partial x_1} \tag{39}$$

$$\frac{\partial h}{\partial x_2} = \sum_{j=1}^{N} \lambda_j \frac{\partial \psi}{\partial x_2} + \sum_{j=1}^{n} \lambda_{N+j} \frac{\partial^2 \psi}{\partial \xi_1 \partial x_2} + \sum_{j=1}^{n} \lambda_{N+n+j} \frac{\partial^2 \psi}{\partial \xi_2 \partial x_2} + \sum_{j=1}^{n^{\mathrm{cl}}} \lambda_{N+n+n+j} \left(n_{\xi_1} \frac{\partial^2 \psi}{\partial \xi_1 \partial x_2} + n_{\xi_2} \frac{\partial^2 \psi}{\partial \xi_2 \partial x_2} \right) + \frac{\partial P_2(\mathbf{x})}{\partial x_2} \tag{40}$$

DOI: 10.1002/fld

The RBF interpolation forms a matrix representation $\eta_i = A_{ij}\lambda_j$ to be solved for the unknowns λ_j. Matrix A_{ij} and vector η_i are given by,

$$A_{ij} = \begin{pmatrix} \psi & \dfrac{\partial\psi}{\partial\xi_1} & \dfrac{\partial\psi}{\partial\xi_2} & n_{\xi_1}\dfrac{\partial\psi}{\partial\xi_1} + n_{\xi_2}\dfrac{\partial\psi}{\partial\xi_2} & P_2 \\ \dfrac{\partial\psi}{\partial x_1} & \dfrac{\partial^2\psi}{\partial\xi_1\partial x_1} & \dfrac{\partial^2\psi}{\partial\xi_2\partial x_1} & n_{\xi_1}\dfrac{\partial^2\psi}{\partial\xi_1\partial x_1} + n_{\xi_2}\dfrac{\partial^2\psi}{\partial\xi_2\partial x_1} & \dfrac{\partial P_2}{\partial x_1} \\ \dfrac{\partial\psi}{\partial x_2} & \dfrac{\partial^2\psi}{\partial\xi_1\partial x_2} & \dfrac{\partial^2\psi}{\partial\xi_2\partial x_2} & n_{\xi_1}\dfrac{\partial^2\psi}{\partial\xi_1\partial x_2} + n_{\xi_2}\dfrac{\partial^2\psi}{\partial\xi_2\partial x_2} & \dfrac{\partial P_2}{\partial x_2} \\ A^1 & A^2 & A^3 & A^4 & A^5 \\ (P_2)^{\mathrm{T}} & \left(\dfrac{\partial P_2}{\partial x_1}\right)^{\mathrm{T}} & \left(\dfrac{\partial P_2}{\partial x_2}\right)^{\mathrm{T}} & (A^5)^{\mathrm{T}} & 0 \end{pmatrix} \tag{41}$$

Terms A^1–A^5 are given by

$$A^1 = n_{x_1}\frac{\partial\psi}{\partial x_1} + n_{x_2}\frac{\partial\psi}{\partial x_2} \tag{42}$$

$$A^2 = n_{x_1}\frac{\partial^2\psi}{\partial\xi_1\partial x_1} + n_{x_2}\frac{\partial^2\psi}{\partial\xi_1\partial x_2} \tag{43}$$

$$A^3 = n_{x_1}\frac{\partial^2\psi}{\partial\xi_2\partial x_1} + n_{x_2}\frac{\partial^2\psi}{\partial\xi_2\partial x_2} \tag{44}$$

$$A^4 = n_{x_1}\left(n_{\xi_1}\frac{\partial^2\psi}{\partial\xi_1\partial x_1} + n_{\xi_2}\frac{\partial^2\psi}{\partial\xi_2\partial x_1}\right) + n_{x_2}\left(n_{\xi_1}\frac{\partial^2\psi}{\partial\xi_1\partial x_2} + n_{\xi_2}\frac{\partial^2\psi}{\partial\xi_2\partial x_2}\right) \tag{45}$$

$$A^5 = n_{x_1}\frac{\partial P_2}{\partial x_1} + n_{x_2}\frac{\partial P_2}{\partial x_2} \tag{46}$$

where $n_{\mathbf{x}^j} = (n_{x_1^j}, n_{x_2^j})$ is the obstacles unit normal at the point $\mathbf{x}^j$. The vector η_i is given by,

$$\eta_i = \left(h \quad \frac{\partial h}{\partial x_1} \quad \frac{\partial h}{\partial x_2} \quad \tan\left(\frac{\pi}{2} - \theta\right) \quad 0\right)^{\mathrm{T}} \tag{47}$$

The RBF yields the position of the element nodal points, the outward unit normal and the curvature. For the case of flow around obstacles, a virtual top is generated to the obstacle and is also interpolated using a RBF as in [9]. This allows the inward unit normal to be found, necessary for evaluating the traction values on this surface, such as in Equation (36).

3. FLOW OVER MULTIPLE HEMISPHERES

Flow profiles over two and three hemispheres are considered in each of the following subsections. For flow over two hemispheres, a range of relative obstacle locations are investigated. For two

DOI: 10.1002/fld

hemispheres located in-line with the flow direction, a parameter analysis is considered, where effects of changing the inverse Bond number $B=\sin^{1/3}\alpha/Bo$, plane inclination angle α, and hemisphere radius a are investigated. Hemispheres that approach the free surface are considered. Finally, this is extended to analyse how the gap between the free surface and obstacle is reduced by interaction of a wake on the flow over a downstream hemisphere.

3.1. Flow over two hemispheres

Flow over two hemispheres spaced symmetrically to the axis by a distance $(x_{1_{\text{sep}}}, x_{2_{\text{sep}}})$ is considered, with the hemisphere centres located at $x_1=\pm x_{1_{\text{sep}}}/2$ and $x_2=\pm x_{2_{\text{sep}}}/2$. Flow is fixed with a Bond number $Bo=1.0$ and is down a plane inclined at $\alpha=45°$, with the two attached hemispheres having radius $a=0.9$. Flow over a single obstacle located at (0,0) has far-field locations $-6\leqslant x_1\leqslant 8$ and $-6\leqslant x_2\leqslant 6$ and for each dual obstacle analysis, the far field is extended from these values as outlined in the previous section.

Figure 4 illustrates the centre line ($x_2=0$) profiles of the free surface in the direction of the upstream flow over two hemispheres in-line with the incident flow and with spacings $x_{1_{\text{sep}}}=2,4,6,8$. Dashed profiles indicate the equivalent flow over a single hemisphere at $(\pm x_{1_{\text{sep}}}/2,0)$. For all cases of obstacle separation, the deformation caused by the upstream hemisphere appears to reproduce closely the corresponding profile for a single obstacle. When the separation is large, the downstream hemisphere of the twin obstacle case reproduces closely the deformation caused by a single obstacle. This is because the wake decays after the upstream obstacle and the incident flow configuration to the downstream obstacle approximates an undisturbed flow. As the obstacles are moved closer together the profile over the rear hemisphere is distorted more, with the peak decreasing and the trough increasing in amplitude. For $x_{1_{\text{sep}}}\geqslant 4$, the flow over the rear obstacle appears as a complete profile, rising from around the undisturbed flow height towards a peak and decaying behind the obstacle. For $x_{1_{\text{sep}}}=2$, the profile fundamentally changes and the flow over the rear obstacle begins during the collapse of the peak caused by the upstream obstacle. As such the peaks appear to be joined, with a small step down as flow passes between obstacles. A single, larger trough is formed downstream of the last obstacle, instead of behind each hemisphere in turn. This is confirmed by the contour plot in Figure 7 for $x_{1_{\text{sep}}}=2$, $x_{2_{\text{sep}}}=0$.

Figure 5 shows the axis line ($x_1=0$) profiles of the free surface for flow over two hemispheres spaced perpendicular to the incoming flow direction. Dashed profiles correspond to flow over a single hemisphere at $(0,\pm x_{2_{\text{sep}}}/2)$. The obstacle spacing and thus the flow profile is symmetric in each case about the line $x_2=0$. For large separations, the profiles over the two obstacles appear identical to that for a single obstacle. As the obstacles are moved closer, the outer regions of the flow profiles remain consistent with the corresponding single obstacle solution. For $x_{2_{\text{sep}}}\geqslant 4$, the inner region of the profiles merges with the lowest surface point between hemispheres increasing from the undisturbed film height. In these cases, the peak height above each hemisphere is of similar magnitude to the single hemisphere case. For $x_{2_{\text{sep}}}=2$, the two profiles merge producing a single peak, much taller than that created for a single obstacle. The resultant cross-section flow profile appears as if the flow is interacting with a single larger obstacle. The contour plot in Figure 7 for $x_{1_{\text{sep}}}=0, x_{2_{\text{sep}}}=2$ confirms this.

Figure 6 indicates the obstacle and the free surface meshes for the analysis of flow over two hemispheres separated by $x_{1_{\text{sep}}}=x_{2_{\text{sep}}}=2$ and with centres located at $(-1,-1)$ and (1,1). The flow is incident to the leading hemisphere, and as the peak splits into a typical horseshoe shape, one

DOI: 10.1002/fld

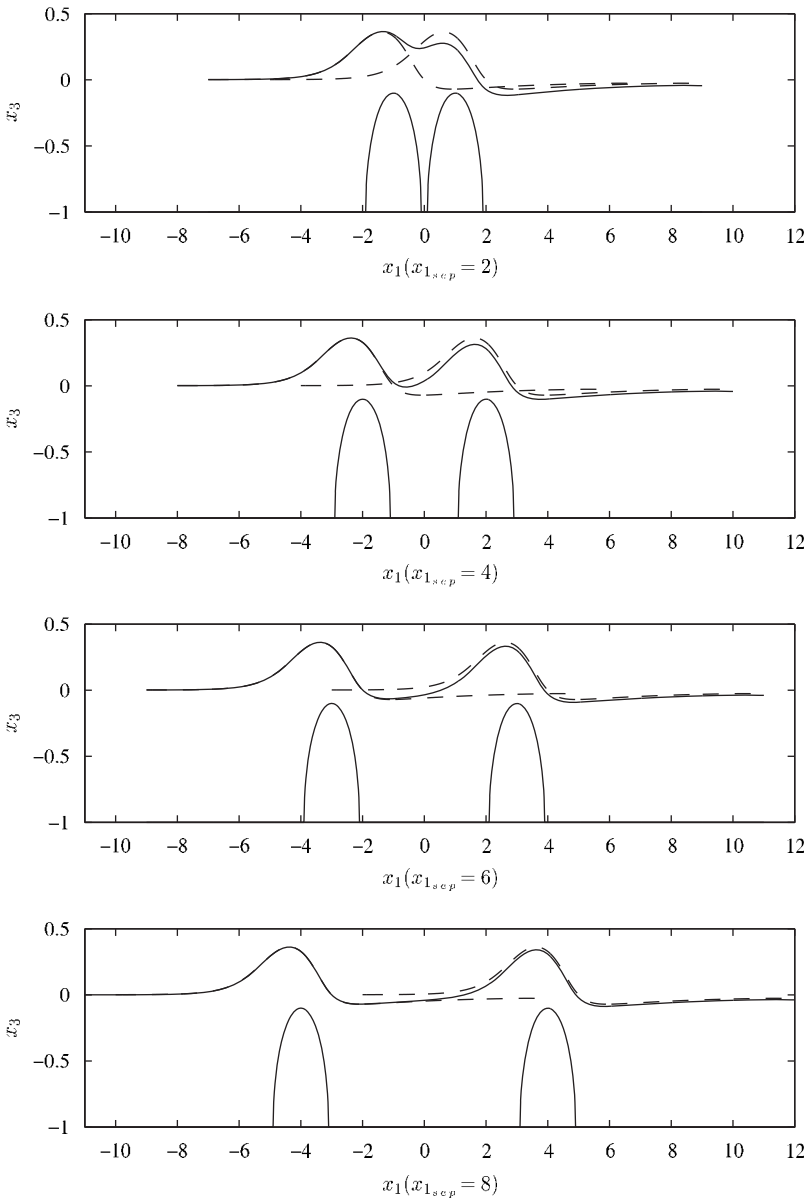

Figure 4. Centre line profiles for hemisphere separation distances $x_{1_{\text{sep}}} = 2$, 4, 6, and 8 in-line with the flow.

of the raised ridges is incident to the downstream hemisphere. This thicker film region causes the peak over the rear hemisphere to be even taller, before decaying in a typical fashion. The close proximity of the two obstacles allows most of the peaks to merge, with only the tips of the two deflections left independent. This is illustrated further by the contour plot in Figure 7 for $x_{1_{\text{sep}}} = 2$, $x_{2_{\text{sep}}} = 2$.

DOI: 10.1002/fld

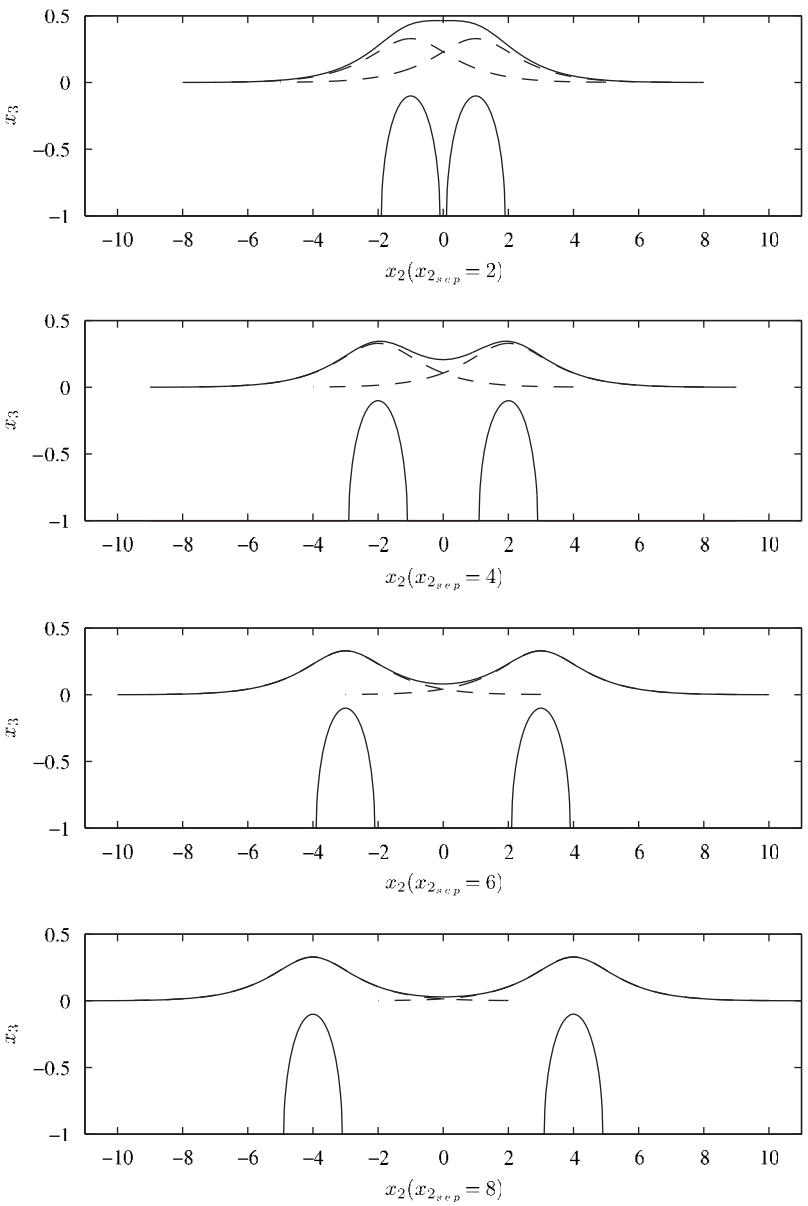

Figure 5. Centre line profiles for hemisphere separation distances $x_{2_{\text{sep}}} = 2$, 4, 6, and 8 perpendicular to the flow.

Figure 7 shows three comparison contour plots for the obstacle configurations corresponding to Figures 4–6. Clearly, for $x_{1_{\text{sep}}} = 2$, $x_{2_{\text{sep}}} = 0$ the flow is symmetric in $x_2 = 0$ and the highest point on the free surface occurs just prior to the leading hemisphere. The peak is continued over the rear hemisphere and then collapses rapidly into a trough around $x_1 = 1.5$. This can also be seen in the

DOI: 10.1002/fld

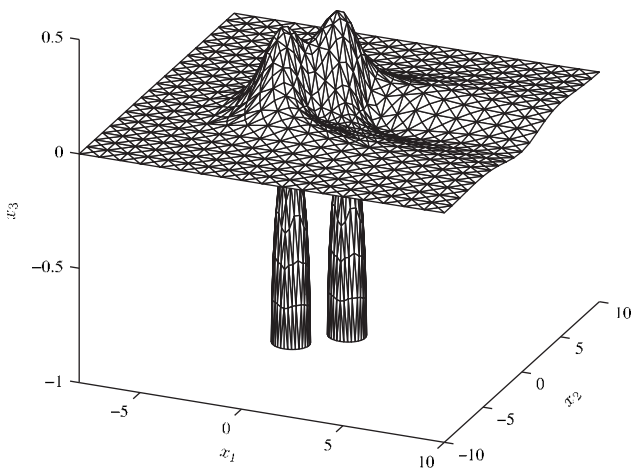

Figure 6. 3D solution profile for two hemispheres separated by $x_{1_{\text{sep}}} = 2$, $x_{2_{\text{sep}}} = 2$.

centre line plot in Figure 4. The contour plot for $x_{1_{\text{sep}}} = 0$, $x_{2_{\text{sep}}} = 2$ again illustrates the symmetry in $x_2 = 0$, with just a single, wide peak occurring over $x_2 = 0$. This is also seen in Figure 5. The peak decays rapidly into the trough just behind the line of the obstacles. However, the contour lines are disturbed downstream slightly along $x_2 = 0$ during the formation of the trough. In this case the flow is forced between the obstacles extending the peak region slightly. The contour plot for the two off-set hemispheres of Figure 6 does not show symmetry in the line $x_2 = 0$. In this case the peaks that occur due to the two obstacles can be clearly seen, with the downstream peak slightly larger. The rear hemisphere is clearly seen to lie in the decaying peak of the flow profile about the upstream hemisphere causing an extension to the distance that the raised ridge is noticed downstream.

3.1.1. Parameter analysis. A parameter investigation is conducted for flow over two hemispheres aligned with the incident flow and separated by $x_{1_{\text{sep}}} = 2$. The effects of changed inverse Bond number B, plane inclination angle α, and differential obstacle radii a are considered. Default values for the flow parameters include an inverse Bond number of $B = 1$, a plane inclination angle of $\alpha = 45°$, and hemispheres of radii $a = 0.9$. In each case two parameters are chosen from above and the effects of altering the third analysed.

Figure 8 illustrates the centre line ($x_2 = 0$) solutions for variations of inverse Bond number B. The increase in B, associated with an increase in surface tension forces, results in the flattening and smoothing of the profiles. For $B = 1$, the centre line profiles appear to oscillate as they pass from the first to the second hemisphere, forming two local peaks and a trough. The increase in B acts to smooth these local peaks, which subsequently merge to form a single ridge that spans across the two obstacles. Consistent with the single obstacle analysis in Baxter *et al.* [9], the inverse Bond number causes the height of the peak to reduce and for the disturbance to span a greater region upstream in the x_1 direction.

Figure 9 illustrates centre line ($x_2 = 0$) solutions for a range of plane inclination angles α with two local peaks occurring over each obstacle for all plane angles. The trough appears to shift slightly upstream, towards the back edge of the second hemisphere as the plane angle is reduced.

DOI: 10.1002/fld

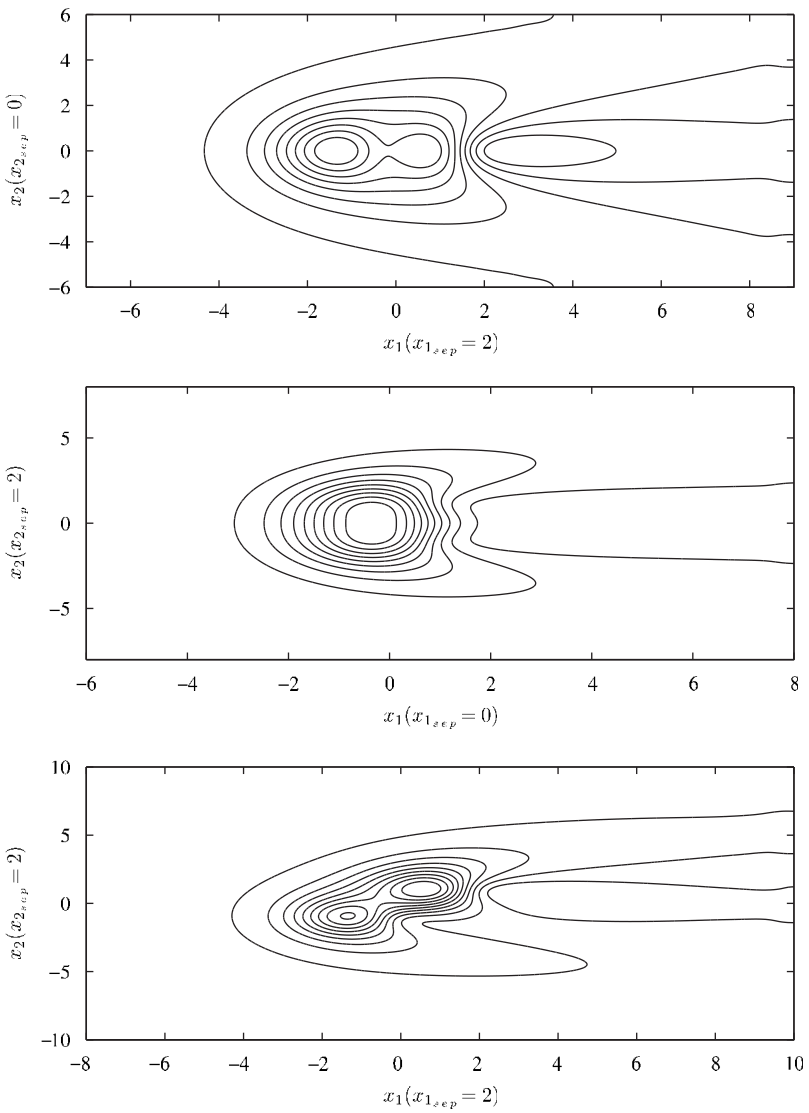

Figure 7. Contour plots for $(x_{1_{\text{sep}}}, x_{2_{\text{sep}}}) = (2,0),(0,2),(2,2)$.

Consistent with the single obstacle case, the steeper the plane wall, the larger the peak that is formed.

Figure 10 gives the centre line ($x_2 = 0$) profiles for flow over two hemispheres separated by $x_{1_{\text{sep}}} = 2$ and with three differential radii; $a = 0.5$, 1.3, $a = 0.9$, 0.9, and $a = 1.3$, 0.5. When the obstacles are the same size ($a = 0.9, 0.9$), the flow exhibits two local peaks and a trough as the flow passes from the leading to the rear hemisphere. For the case of a small obstacle followed by a large obstacle ($a = 0.5, 1.3$), the flow appears to climb relatively slowly to a single peak over the

DOI: 10.1002/fld

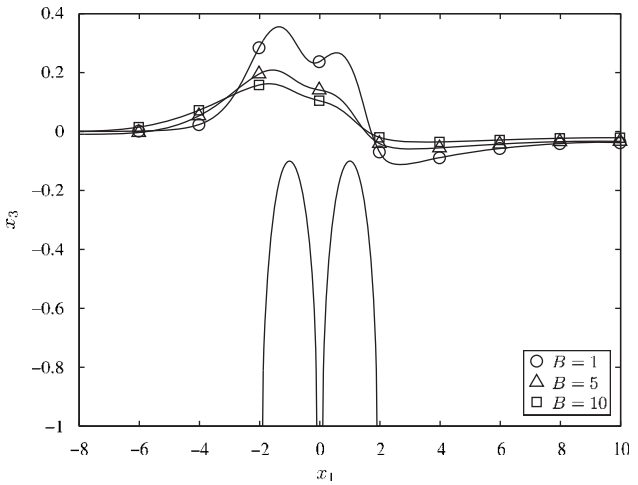

Figure 8. Centre line solution profiles for two hemispheres separated by $x_{1_{\text{sep}}} = 2$, indicating the effect of varying the inverse Bond number B.

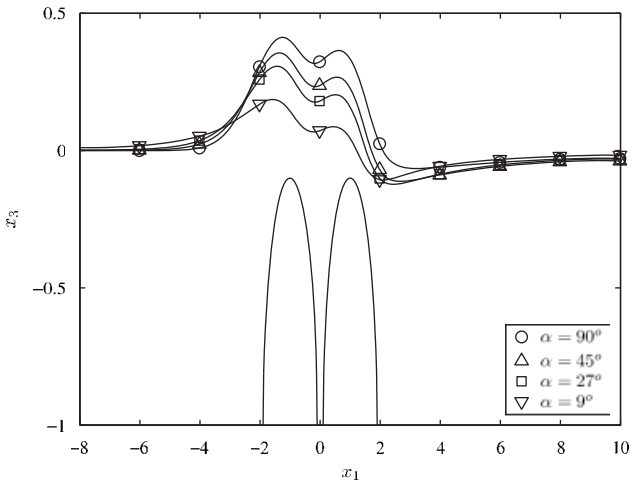

Figure 9. Centre line solution profiles for two hemispheres separated by $x_{1_{\text{sep}}} = 2$, showing the effect of varying the plane inclination angle α.

downstream obstacle. For the case of a large obstacle followed by a small obstacle ($a = 1.3, 0.5$), the flow exhibits a large peak over the leading obstacle. However, in this case the formation of the trough shows a small kink over the rear obstacle. Interestingly the maximum peak heights for both cases of different sized hemispheres are approximately equal, and significantly greater than the case of equal hemisphere size; this suggests that the peak height is strongly dependent on the maximum hemisphere radius. The corresponding film height for flow over a single hemisphere of radius $a = 1.3$ is provided allowing comparison with the dual hemisphere solution. When the large

DOI: 10.1002/fld

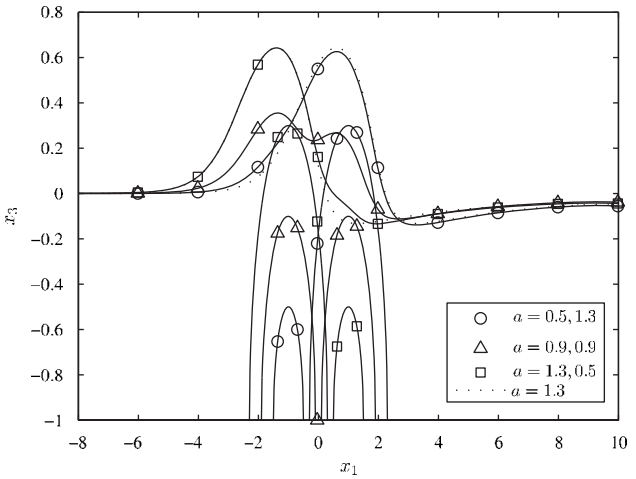

Figure 10. Centre line solution profiles for two hemispheres separated by $x_{1_{\text{sep}}} = 2$, indicating the effect of varying the two obstacles radii a. Dotted lines indicate a single hemisphere of radius $a = 1.3$.

Table II. Near-point values (3.s.f.) for large hemispheres on shallow and steep planes.

	Shallow ($\alpha = 5°$) plane with $a = 1.05$	Steep ($\alpha = 90°$) plane with $a = 1.60$
Single	0.0486	0.337
Double	0.0465	0.220

hemisphere precedes the small hemisphere, flow over this obstacle shows negligible discrepancy to the single case. When the large hemisphere is the rear obstacle, a small difference to the single obstacle solution is present.

Baxter *et al.* [9] found that the largest possible hemisphere containable within the fluid film was strongly dependent on the inclination of the plane. Profiles have been compared for a Bond number $Bo = 1$ and obstacle separation $x_{1_{\text{sep}}} = 4$, $x_{2_{\text{sep}}} = 0$. Table II indicates the smallest distance between the interpolated free surface and the obstacle for both a single and dual hemisphere configuration. Results on both the shallow and steep plane show this minimum distance is reduced when two obstacles are considered. For the shallow plane, hemispheres of radius $a = 1.05$ are modelled and only a minor reduction is noticed, as shown in Figure 11. For the steep plane, hemispheres of radius $a = 1.60$ are modelled and a significant reduction in the free surface/obstacle gap is found, as shown in Figure 12. It is noted that the results in [9] are found using a different mesh for the same flow parameters as the results here, and this accounts for small differences in solutions.

Centre line profiles for flow down a shallow plane corresponding to Table II are shown in Figure 11. Flow is down a plane inclined at $\alpha = 5°$, and a minor reduction in the gap between the obstacle and free surface is found behind the rear hemisphere when compared with a single obstacle analysis. Centre line solutions for flow down a steep plane corresponding to the information in Table II are shown in Figure 12. Flow is down a plane inclined at $\alpha = 90°$, and a significant

DOI: 10.1002/fld

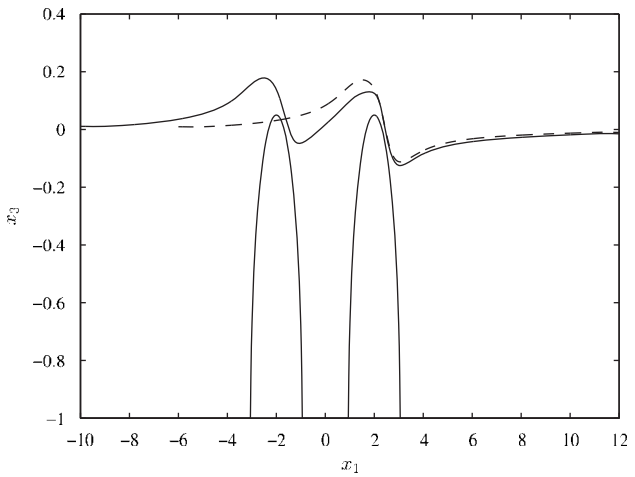

Figure 11. Centre line solution for large hemispheres on a shallow plane at $\alpha = 5°$ over hemispheres of radius $a = 1.05$. Comparison is shown with a single hemisphere.

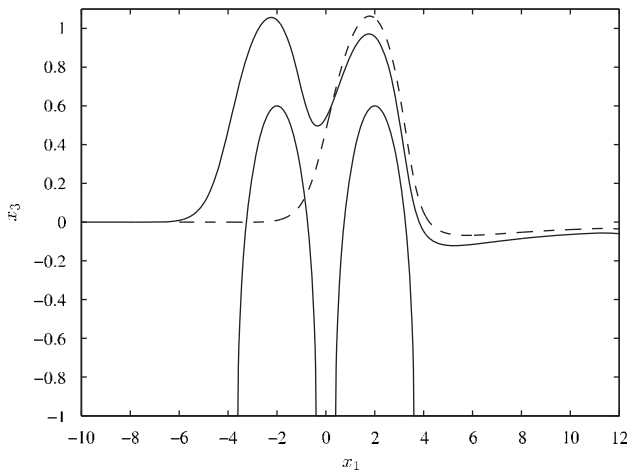

Figure 12. Centre line solution for large hemispheres on a steep plane at $\alpha = 90°$ over hemispheres of radius $a = 1.60$. Comparison is shown with a single hemisphere.

reduction in the near-point values between the obstacle and free surface is found behind the rear hemisphere obstacle when compared with a single obstacle analysis.

3.2. Flow over three hemispheres

Illustration of flow over three hemispheres is now given for two obstacle configurations. Flow has a Bond number $Bo = 1$, all hemispheres have a radius of $a = 0.9$, and the plane is inclined at $\alpha = 45°$. Obstacles are positioned in a symmetrical triangular array, with either a twin or single leading

DOI: 10.1002/fld

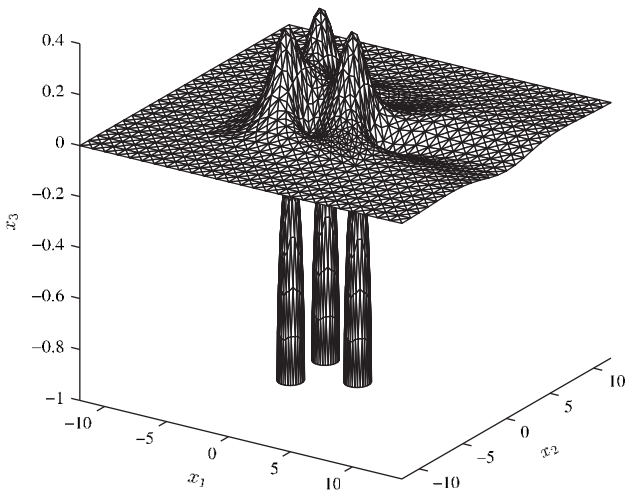

Figure 13. 3D solution profile for three hemispheres located at $(-2,-2)$, $(-2,2)$, (2,0).

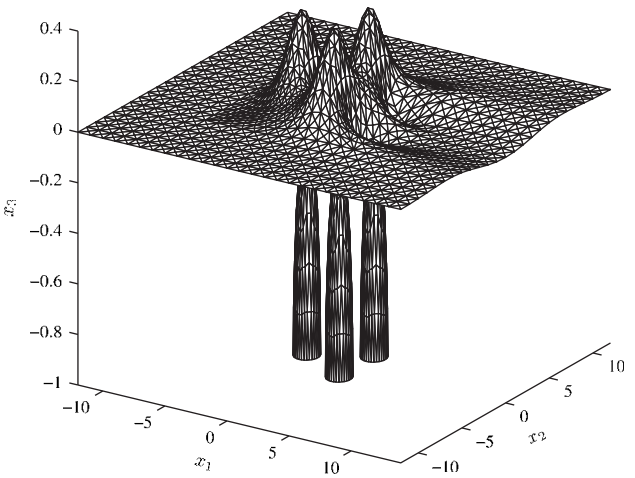

Figure 14. 3D solution profile for three hemispheres located at $(-2,0)$, $(2,-2)$, (2,2).

hemisphere configuration considered. A twin leading configuration is illustrated in Figure 13 and consists of the upstream flow incident on two obstacles spaced perpendicularly to the flow direction with centres $(-2,-2)$, $(-2,2)$. This is followed by a trailing hemisphere centred at (2,0). The configuration shown in Figure 14 consists of the upstream flow incident on one obstacle centred at $(-2,0)$ followed by two downstream hemispheres spaced perpendicularly to the flow direction with centres at $(2,-2)$, $(2,2)$. In both cases, three peaks are clearly seen just prior to each obstacle.

DOI: 10.1002/fld

4. FLOW AROUND MULTIPLE CYLINDERS

Profiles for flow around two and three circular cylinders are considered in the following subsections. For flow around two cylinders, a range of relative obstacle locations is considered. For two cylinders lying in-line with the flow direction, a parameter analysis is considered, where effects of changing the inverse Bond number B, plane inclination angle α, cylinder radius a, and contact angle θ are investigated. Finally, cases where flow passes over the first cylinder, but due to the formation of a wake, passes around an identical cylinder further downstream, are considered.

4.1. Flow around two cylinders

Comparison of flow around two cylinders, of equal radius $a=1.0$ and spaced symmetrically with respect to the axis by $(x_{1_{\text{sep}}}, x_{2_{\text{sep}}})$ is considered with the cylinders centred on $(\pm x_{1_{\text{sep}}}/2, x_{2_{\text{sep}}}/2)$. Flow in each case has a Bond number $Bo=1.0$ and is down a plane inclined at $\alpha=45°$. A contact angle condition of $\theta=90°$ is prescribed. Flow around a single cylinder located at (0,0) has far-field locations $-8\leqslant x_1\leqslant 13$ and $-8\leqslant x_2\leqslant 8$ and this is extended similarly to that described in the previous section for flow over two hemispheres.

Figure 15 illustrates the centre line ($x_2=0$) profiles for flow around two cylinders in-line with the incident flow and with various spacings. Comparison profiles are given for flow around a single cylinder at $(\pm x_{1_{\text{sep}}}/2, 0)$. For all cases of obstacle separation, the flow profile generated by the upstream cylinder appears to reproduce closely the profile for a single cylinder. When the separation is increased, flow around the downstream cylinder approximates more closely the deformation caused by a single obstacle. As the separation increases, the wake decays after the leading cylinder and the incident flow configuration to the rear obstacle approaches that of an undisturbed flow. As the obstacles are moved closer together the peak height incident on the rear cylinders wall decreases. For $x_{1_{\text{sep}}}\geqslant 6$, the flow around the rear obstacle stems from the same location on the back edge of the upstream cylinder. The flow height on the back edge of the downstream cylinder is slightly reduced as the obstacles are brought closer together, although any changes are small. For $x_{1_{\text{sep}}}=4$, the profile fundamentally changes, with the film height on the back edge of the upstream cylinder raised significantly, and the film height at the upstream edge of the rear cylinder lowered. The flow profile in this case is shown as a contour plot in Figure 18, for $x_{1_{\text{sep}}}=4$ and $x_{2_{\text{sep}}}=0$.

Figure 16 indicates the centre line ($x_1=0$) profiles of flow around two cylinders symmetrically positioned perpendicular to the incoming flow direction. Dashed profiles indicate the flow profiles around a single cylinder at $(0, \pm x_{2_{\text{sep}}}/2)$. For large separations ($x_{2_{\text{sep}}}\geqslant 6$), the profiles around the double obstacle are accurately approximated by the flow profiles for two single obstacles, with the outer regions of the flow profiles remaining consistent with the corresponding single obstacle solution. The lowest free surface height in the merged inner region of the flow slowly increases from the undisturbed film height as the cylinders are brought closer together. For $x_{2_{\text{sep}}}=4$, the outer regions of the profile show changes raising the contact point on the cylinder wall. The film height of the inner region is raised significantly as the flow is forced through the small gap between the cylinders. A contour plot of this profile is shown in Figure 18, for $x_{1_{\text{sep}}}=0$ and $x_{2_{\text{sep}}}=4$.

Figure 17 indicates the free surface mesh for the analysis of flow around two off-set cylinders separated by $x_{1_{\text{sep}}}=x_{2_{\text{sep}}}=4$. The flow is incident to the first cylinder, and as the flow peak splits around the obstacle, one of these raised ridges is incident onto the downstream cylinder. This thicker film region causes the peak formed around the rear cylinder to increase, before decaying with a typical wake structure for a single cylinder. The individual profiles around each cylinder are

DOI: 10.1002/fld

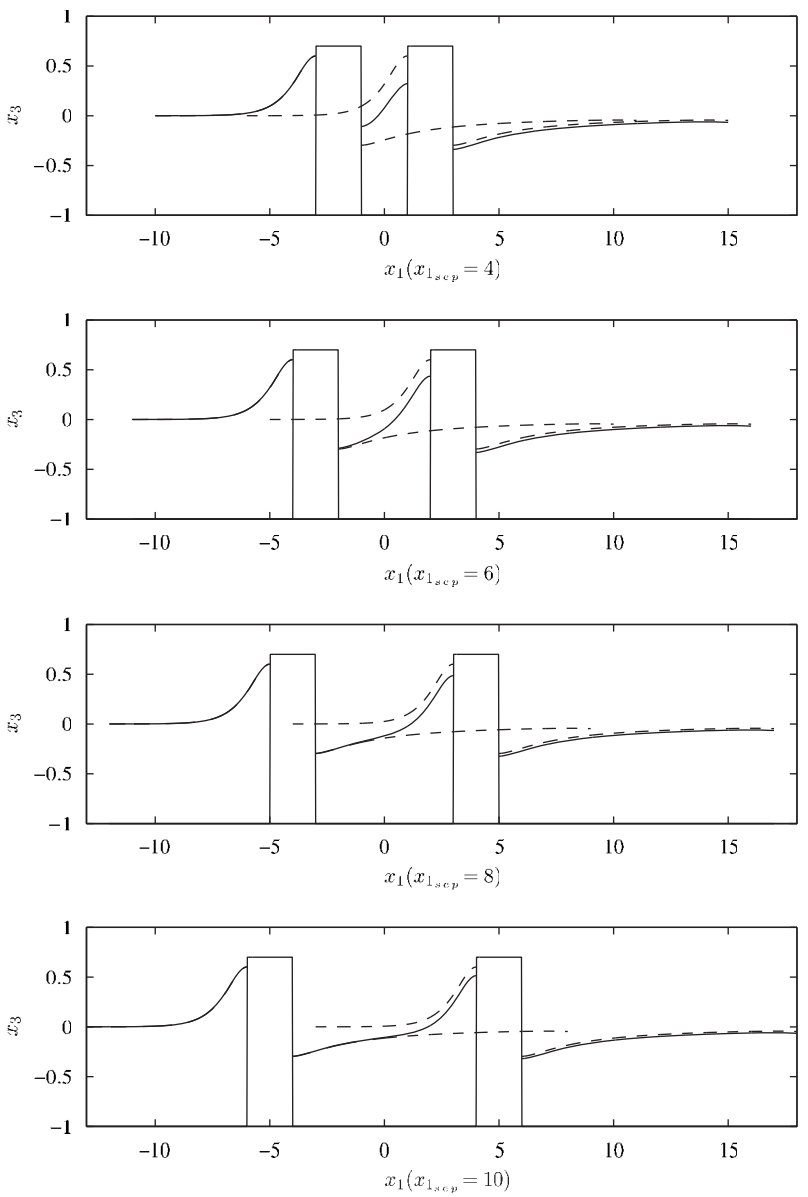

Figure 15. Centre line profiles for various cylinder separation distances $x_{1_{\text{sep}}}$ in-line with the flow. Comparison with results for a single cylinder are shown with a dashed line.

sufficiently close to exhibit interaction with each other as is illustrated by the associated contour plot in Figure 18.

Figure 18 illustrates three contour plots for the obstacle configurations corresponding to Figures 15–17. Taking $x_{1_{\text{sep}}} = 4$, $x_{2_{\text{sep}}} = 0$, the flow is symmetric in $x_2 = 0$ and the highest points

DOI: 10.1002/fld

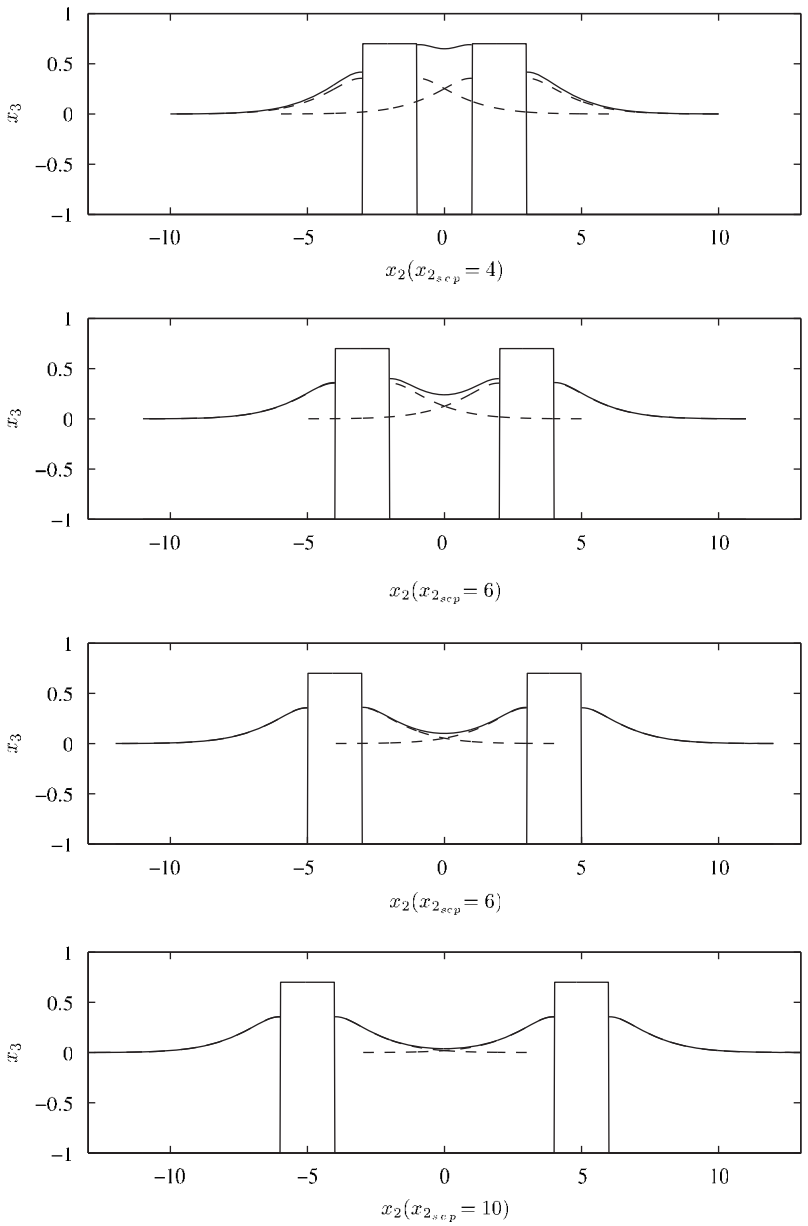

Figure 16. Centre line profiles for various cylinder separation distances $x_{2_{\text{sep}}}$ perpendicular to the flow. Comparison with results for a single cylinder are shown with a dashed line.

on the free surface occur on the upstream edge of the two cylinders. The rapid rise in film height is shown between the two cylinders as the trough from the leading cylinder develops into the peak of the downstream obstacle. The centre line plot for this flow can also be seen in Figure 15.

DOI: 10.1002/fld

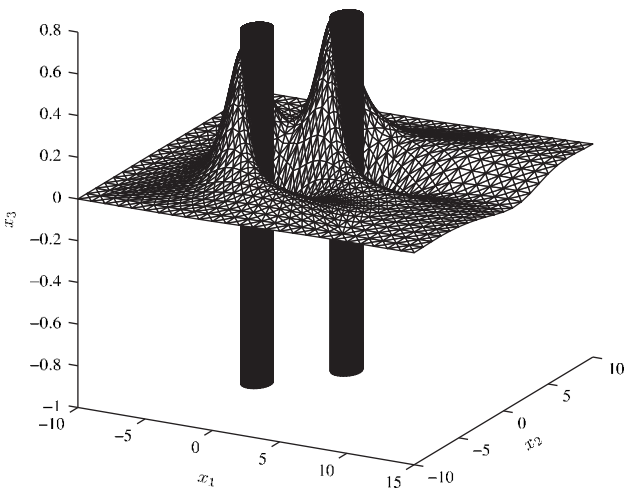

Figure 17. 3D solution profile for two cylinders separated by $x_{1_{\text{sep}}}=4$, $x_{2_{\text{sep}}}=4$.

The contour plot for the case $x_{1_{\text{sep}}}=0$, $x_{2_{\text{sep}}}=4$ illustrates just a single, wide peak occurring and covering the leading edges of the two cylinders. The peak decays into a trough just behind each of the cylinders, with the raised flow forced between the cylinders decaying to the undisturbed film height further downstream. The contour plot for the non-symmetric case $x_{1_{\text{sep}}}=4$, $x_{2_{\text{sep}}}=4$ shows the contours of flow around two off-set cylinders with the downstream cylinder generating a slightly larger peak. The rear cylinder is seen to lie in the decaying peak of the upstream cylinder causing the range of this peak to extend further downstream.

4.1.1. Parameter analysis. A parameter analysis is conducted demonstrating the effects of altering the inverse Bond number B, plane inclination angle α, obstacle radii a, and contact angle θ. An in-line configuration with $x_{1_{\text{sep}}}=8$ is taken. Default values for the flow parameters include an inverse Bond number of $B=1$, a plane inclination angle of $\alpha=45°$, circular cylinders of radius $a=1.0$, and a contact angle condition of $\theta=90°$. In each case, three parameters are chosen from above and the effects of altering the fourth analysed.

Figure 19 illustrates the centre line ($x_2=0$) solutions for variations in inverse Bond number with an increase in B showing a flattening and smoothing of the profiles associated with an increase in surface tension. For $B=1$, the centre line profiles undergo large variations in film height. The effects of increasing B are to raise the lowest points and lower the highest points of the film, minimizing the deformation of the free surface. In common with the single obstacle analysis of Baxter *et al.* [9] and the earlier dual hemisphere analysis, the inverse Bond number causes the film disturbance to span a greater region upstream in the x_1 direction.

Figure 20 illustrates centre line ($x_2=0$) solutions for changes to the plane inclination angles α. It is noted that the steeper the plane wall, the larger the peak that is formed on the cylinders. Interestingly, the larger cylinders analysed here when compared with the results in Baxter *et al.* [9] show the film height on the downstream edge of the cylinder to be raised as the plane angle is decreased. This is in contrast to the single cylinder results of [9], which showed the downstream location to be close for all plane angles and not monotonic.

DOI: 10.1002/fld

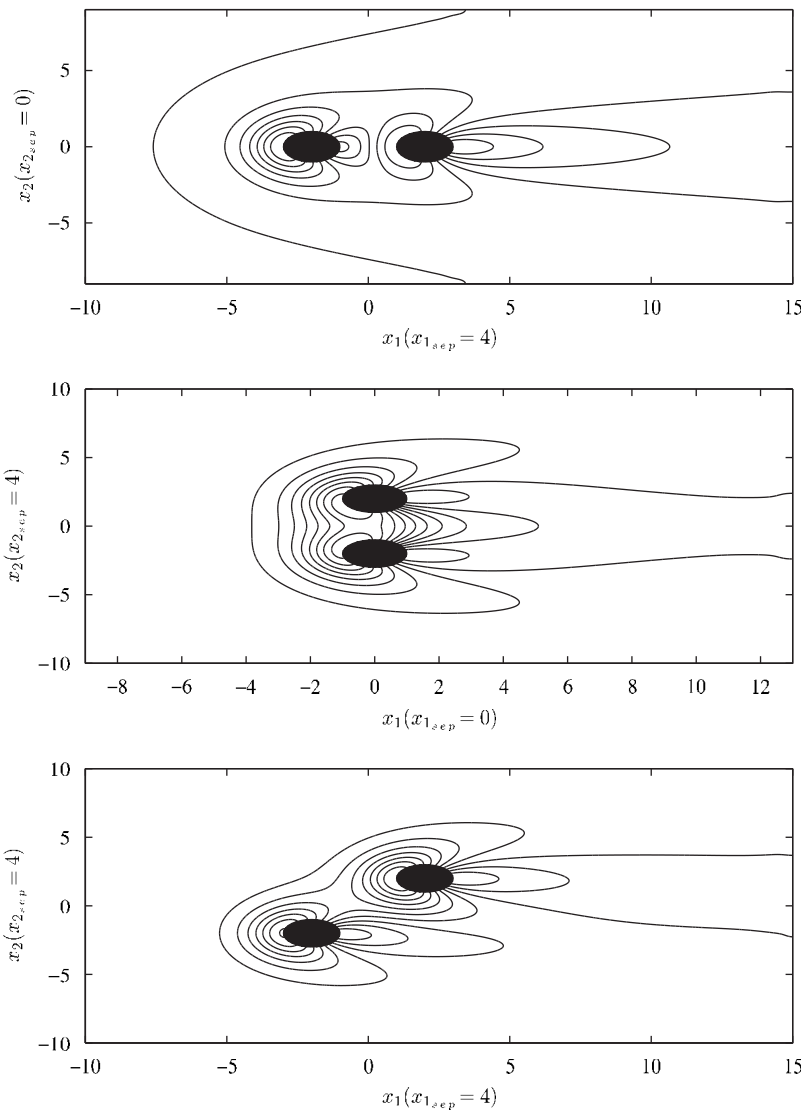

Figure 18. Contour plots for $(x_{1_{\text{sep}}}, x_{2_{\text{sep}}}) = (4, 0), (0, 4), (4, 4)$.

Figure 21 shows the centre line ($x_2 = 0$) profiles for variations in cylinder radius. Larger cylinders cause greater deformations of the free surface with increasing peak and decreasing trough heights around the upstream cylinder. In addition, the trough of the downstream cylinder is lowered with increasing cylinder radius. The corresponding peak at the downstream cylinder for successive heights $a = 0.5$, 1.0, 1.5 is increased; however, the peak height on the centre line associated with $a = 2.0$ is actually lower than the corresponding height for $a = 1.5$. In this latter case the deeper

DOI: 10.1002/fld

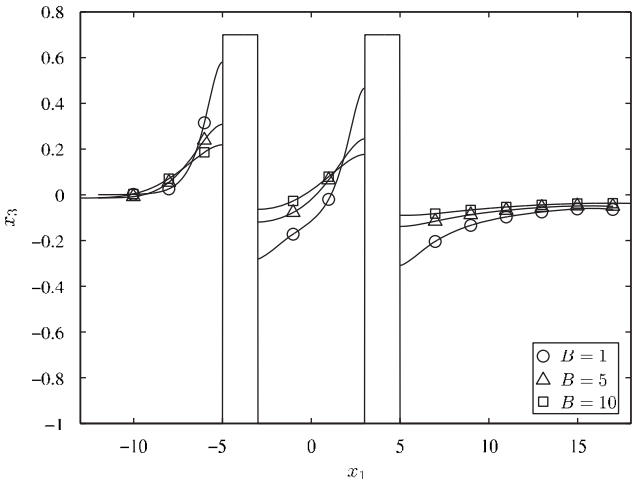

Figure 19. Centre line solution profiles for two cylinders separated by $x_{1_{\text{sep}}} = 8$, indicating the effects of varying the inverse Bond number B.

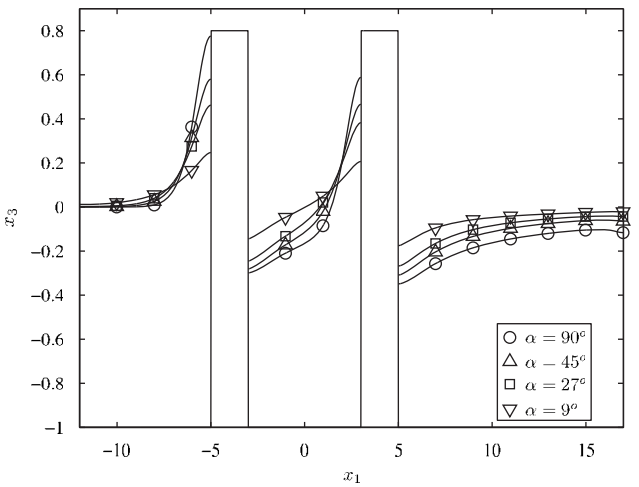

Figure 20. Centre line solution profiles for two cylinders separated by $x_{1_{\text{sep}}} = 8$, indicating the effects of varying the plane inclination angle α.

trough behind the upstream cylinder, associated with $a = 2.0$, forces the peak at the downstream cylinder to be reduced due to the large variation in film height necessary.

Figure 22 indicates the centre line ($x_2 = 0$) profiles for variations in the contact angle at the cylinder/free surface interface. Results show the profiles are altered significantly depending on whether a wetting or non-wetting condition is applied at the cylinder. It is interesting to note that the global effect of this local parameter variation. When a wetting condition is applied i.e. $\theta < 90°$, the peaks maximize at the cylinder wall, and the minimum flow height is found a small distance

DOI: 10.1002/fld

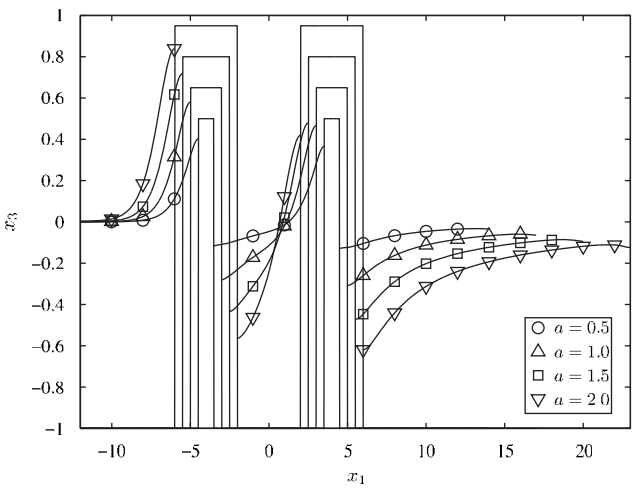

Figure 21. Centre line solution profiles for two cylinders separated by $x_{1_{\text{sep}}} = 8$, indicating the effects of varying the cylinders radii a.

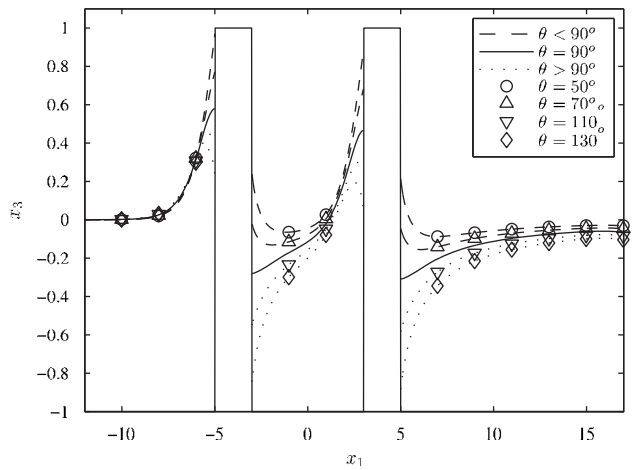

Figure 22. Centre line solution profiles for two cylinders separated by $x_{1_{\text{sep}}} = 8$, indicating the effects of varying the static contact line angle θ.

from the cylinder. For non-wetting cylinders i.e. $\theta > 90°$, the peak heights occur away from the cylinder wall and the flow height minimizes at the point of contact. These results are consistent with the case of a single cylinder [9].

4.2. Flow around three cylinders

The flow around three cylinders in two geometrical configurations is considered. Flow is taken down a plane inclined at $\alpha = 45°$ and has a Bond number $Bo = 1$. Flow is around circular cylinders

DOI: 10.1002/fld

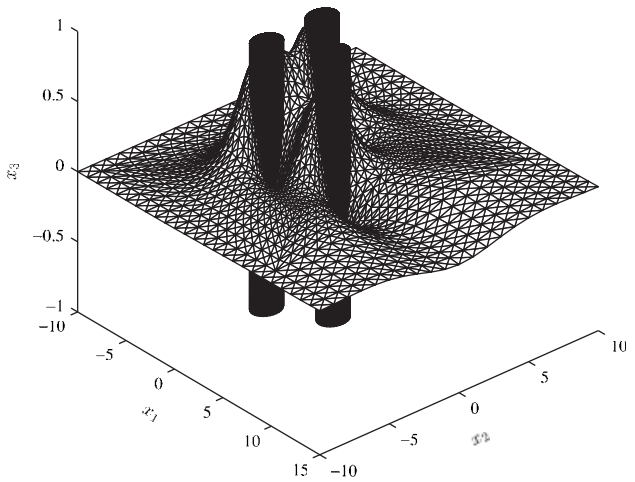

Figure 23. 3D solution profile for three cylinders located at $(-2, 2)$, $(-2, -2)$, (2,0).

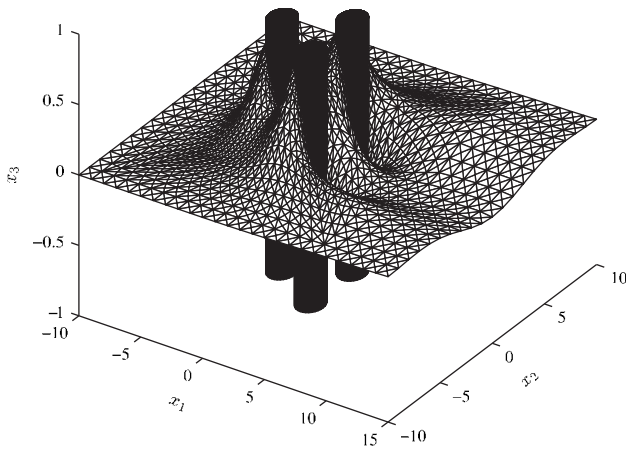

Figure 24. 3D solution profile for three cylinders located at $(-2, 0)$, (2,2), $(2, -2)$.

of radius $a = 1.0$, with a contact angle condition of $\theta = 90°$ applied. Cylinders are positioned in a symmetrical triangular array with either a twin or single leading cylinder considered. A twin leading configuration is illustrated in Figure 23 and consists of the upstream flow incident on two cylinders spaced perpendicularly to the flow direction at centres $(-2, -2)$, $(-2, 2)$. This is followed by a trailing cylinder centred at (2,0). The configuration shown in Figure 24 consists of the upstream flow incident on one obstacle centred at $(-2, 0)$ followed by two downstream cylinders spaced perpendicularly to the flow direction with centres at $(2, -2)$, $(2, 2)$. For both cases, three peaks are clearly seen incident to the upstream edges of each cylinder.

DOI: 10.1002/fld

Table III. Minimum contact angles required for flow to pass around the downstream cylinder.

$x_{1_{sep}}$	Minimum contact angle θ (deg.)
∞	111
8	104
4	100

4.3. Flow over then around a cylinder

The capability of the numerical method is demonstrated by considering the flow configuration of two identical cylinders, aligned in the direction of the flow, where the film passes over the leading cylinder, but due to the surface depression from its wake passes around the downstream cylinder. Flow is down a plane inclined at $\alpha = 90°$, the cylinder radius is $a = 1.0$, and the flow has a Bond number of $Bo = 1.0$. For the rear cylinder, a contact angle is prescribed and minimized while still maintaining the flow to pass around the prescribed cylinder. The upstream cylinder top is sloped linearly in the direction of the flow and meshed as in Baxter *et al.* [9].

This is an extension of the multiple solution work in [9]. If the cylinders separation approaches ∞ in the x_1 direction, then the flow will fully return to its upstream form and the two profiles (over and around the cylinder) can be formed. As the obstacles are brought closer together, the effects of the wake behind the upstream cylinder will act to relax the constraining contact angle condition necessary at the downstream cylinder. A cylinder with a sloped top between $x_3 = 1.60$ at the upstream edge and $x_3 = 1.00$ at the downstream edge is considered. Flow profiles over and around a single cylinder, corresponding to the theoretical case of infinitely spaced cylinders, and double obstacle solutions with spacings $x_{1_{sep}} = 8$ and $x_{1_{sep}} = 4$ are produced. In each case the contact angle θ is minimized while maintaining flow around the prescribed cylinder. Table III indicates the necessary minimum contact angle required to force flow around the downstream cylinder.

Figure 25 indicates four solutions, the first two indicate the centre line solutions for a single obstacle analysis for flow over and around the prescribed cylinder. For multiple solutions to be produced, the contact angle at the cylinder fluid wall is constrained to $\theta \geqslant 111°$. The final two centre lines indicate multiple solutions for flow over then around identical cylinders spaced by finite separations $x_{1_{sep}} = 8$ and 4. As the cylinders are moved closer, the profiles over each obstacle interact more severely and the contact angle condition necessary at the downstream cylinder is reduced.

Figure 26 illustrates the contact lines and cylinder top for the three scenarios for flow around a cylinder depicted in Figure 25. Clearly in each case the flow profiles remain below the cylinder top, and in general as the cylinders are brought closer together, a flattening of the highest region of the profiles occurs.

5. CONCLUSIONS

Numerical solutions for Stokes flow down an inclined plane over and around multiple three-dimensional obstacles have been developed. A general formulation is derived for flow over or

DOI: 10.1002/fld

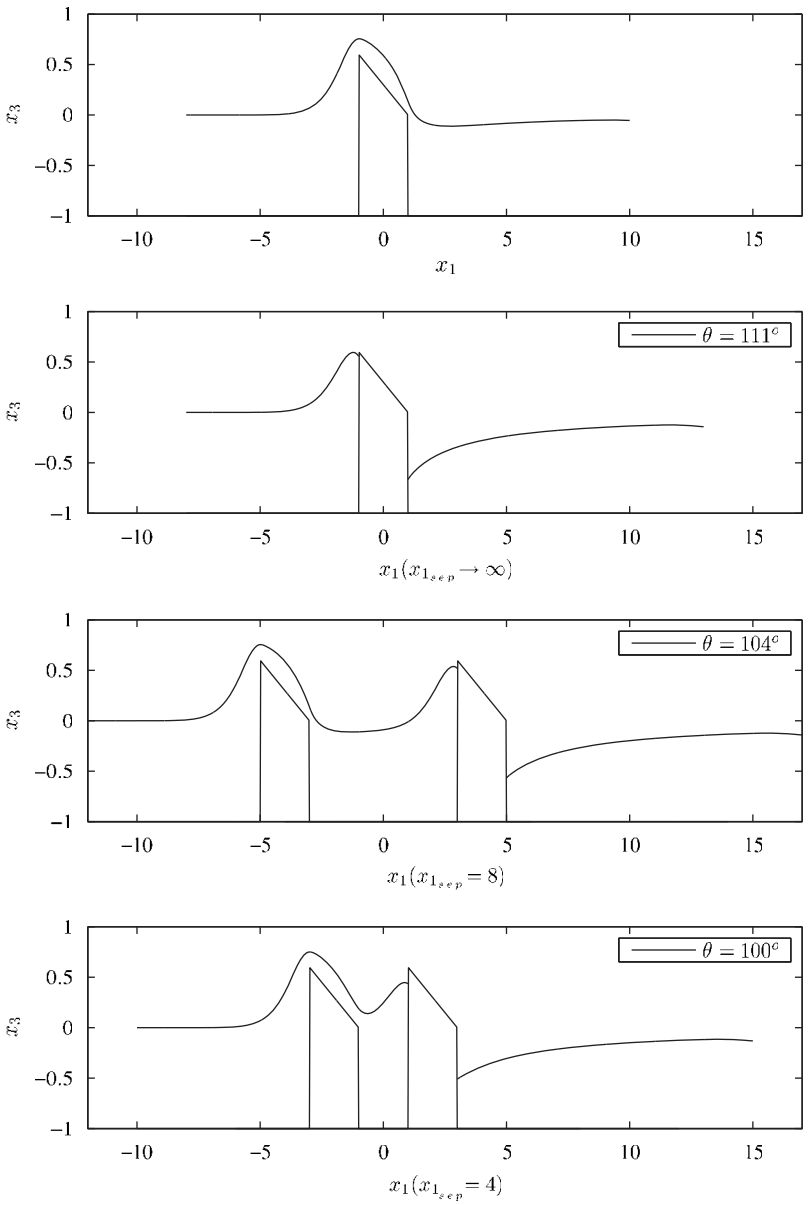

Figure 25. Centre line solution profiles for flow over and around a single cylinder (corresponding to $x_{1\text{sep}} \to \infty$) and for flow over then around two cylinders separated by $x_{1\text{sep}} = 8$ and 4. In each case the contact angle is minimized while maintaining flow around the prescribed cylinder.

around N obstacles, and solutions found via the BEM. Free surface quantities such as curvature and unit normal have been calculated using a RBF interpolation.

Flows over two hemispheres have been considered, with various obstacle locations modelled. For obstacles aligned in the direction of the flow, a parameter study was conducted to investigate

DOI: 10.1002/fld

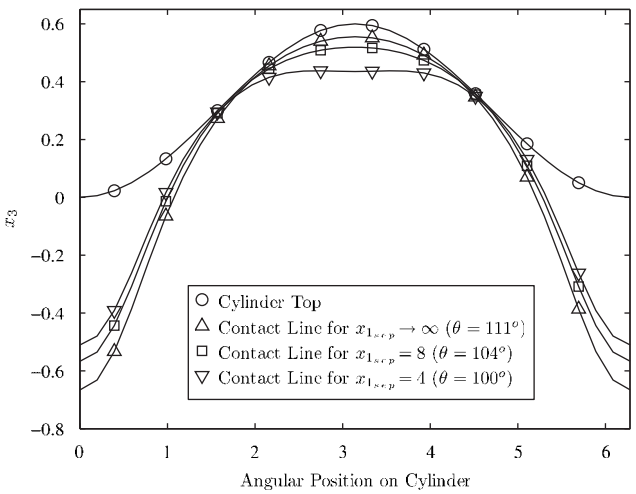

Figure 26. Contact line solutions for flow around each of the cylinders in Figure 25, confirming that flow is always below the top of the cylinder.

the effects of varying the inverse Bond number, plane inclination angle, and hemisphere radius. Flow over two hemispheres that approach the film surface has been modelled, and the effects of placing the downstream obstacle in the wake of the upstream hemisphere considered. The wake from the upstream obstacle on both a shallow and a steep plane is shown to reduce the minimum gap between the free surface and obstacle when compared with a sole obstruction. Finally, flows over three hemispheres were considered, with solutions obtained for two obstacle configurations based on a triangular array.

Flows around two circular cylinders were considered, with various obstacle locations analysed. When the cylinders were aligned in the direction of the flow, a parameter study was conducted to investigate the effects of varying the inverse Bond number, plane inclination angle, cylinder radius, and contact angle. Flow solutions around three cylinders were also considered, with two obstacle configurations based on the triangular array with different symmetrical orientations to the flow direction. Finally, the versatility of the numerical approach is demonstrated with the analysis of a flow over then around two identical cylinders spaced in the direction of the flow. The effect of the wake caused by the upstream cylinder was also considered, and shown to allow the contact angle at the downstream cylinder to be relaxed. As the obstacles are moved closer, the effects of the wake are strengthened and the contact angle condition can be lowered further.

APPENDIX A

The Lorentz–Blake Greens function for semi-infinite flow bounded by an infinite plane wall at $x_3 = w$ is reproduced from Baxter *et al.* [9] and shown below. Throughout the field point is given by $\mathbf{x} = (x_1, x_2, x_3)$ and the singularity point by $\mathbf{x}_0 = (x_{0_1}, x_{0_2}, x_{0_3})$.

DOI: 10.1002/fld

A.1. Lorentz–Blake velocity Greens function

The Lorentz–Blake velocity Greens function, $G^*_{ij}(\mathbf{x}, \mathbf{x}_0)$ is given by,

$$G^*_{ij}(\mathbf{x}, \mathbf{x}_0) = G^{\mathrm{ST}}_{ij}(\hat{\mathbf{x}}) - G^{\mathrm{ST}}_{ij}(\hat{\mathbf{X}}) + 2h_0^2 G^D_{ij}(\hat{\mathbf{X}}) - 2h_0 G^{\mathrm{SD}}_{ij}(\hat{\mathbf{X}}) \tag{A1}$$

where G^{ST}_{ij} is the free-space velocity Greens function or Stokeslet, and

$$G^{\mathrm{ST}}_{ij}(\mathbf{x}) = \frac{\delta_{ij}}{|\mathbf{x}|} + \frac{x_i x_j}{|\mathbf{x}|^3} \tag{A2}$$

$$G^D_{ij}(\mathbf{x}) = \pm\left(\frac{\delta_{ij}}{|\mathbf{x}|^3} - 3\frac{x_i x_j}{|\mathbf{x}|^5}\right) \tag{A3}$$

$$G^{\mathrm{SD}}_{ij}(\mathbf{x}) = x_3 G^D_{ij}(\mathbf{x}) \pm \frac{\delta_{j3}x_i - \delta_{i3}x_j}{|\mathbf{x}|^3} \tag{A4}$$

where a minus corresponds to $j = 3$ and a plus for $j = 1, 2$. Also,

$$h_0 = x_{0_3} - w \tag{A5}$$

$$\hat{\mathbf{x}} = \mathbf{x} - \mathbf{x}_0 \tag{A6}$$

$$\hat{\mathbf{X}} = \mathbf{x} - \mathbf{x}_0^{IM} \tag{A7}$$

$$\mathbf{x}_0^{IM} = (x_{0_1}, x_{0_2}, 2w - x_{0_3}) \tag{A8}$$

A.2. Lorentz–Blake stress Greens function

The Lorentz–Blake stress Greens function, $T^*_{ijk}(\mathbf{x}, \mathbf{x}_0)$ is given by,

$$T^*_{ijk}(\mathbf{x}, \mathbf{x}_0) = T^{\mathrm{ST}}_{ijk}(\hat{\mathbf{x}}) - T^{\mathrm{ST}}_{ijk}(\hat{\mathbf{X}}) + 2h_0^2 T^D_{ijk}(\hat{\mathbf{X}}) - 2h_0 T^{\mathrm{SD}}_{ijk}(\hat{\mathbf{X}}) \tag{A9}$$

where T^{ST}_{ijk} is the free-space stress Greens function, and

$$T^{\mathrm{ST}}_{ijk}(\mathbf{x}) = 6\frac{x_i x_j x_k}{|\mathbf{x}|^5} \tag{A10}$$

$$T^D_{ijk}(\mathbf{x}) = \pm 6\left(-\frac{\delta_{ik}x_j + \delta_{ij}x_k + \delta_{kj}x_i}{|\mathbf{x}|^5} + 5\frac{x_i x_j x_k}{|\mathbf{x}|^7}\right) \tag{A11}$$

$$T^{\mathrm{SD}}_{ijk}(\mathbf{x}) = x_3 T^D_{ijk}(\mathbf{x}) \pm 6\left(\frac{\delta_{ik}x_j x_3 - \delta_{j3}x_i x_k}{|\mathbf{x}|^5}\right) \tag{A12}$$

where a minus corresponds to $j = 3$ and a plus for $j = 1, 2$. Also h_0, $\hat{\mathbf{x}}$, $\hat{\mathbf{X}}$, $\mathbf{x}_0^{IM}$ are defined by (A5)–(A8), respectively.

ACKNOWLEDGEMENTS

This research was carried out at the University Technology Centre in Gas Turbine Transmission Systems at the University of Nottingham with financial support from Rolls-Royce plc, Aerospace Group, and the

DOI: 10.1002/fld

Technology Strategy Board via WP14 (Management of Complex fluid flow conditions) of Project CFMS. The views expressed in this paper are those of the authors and not necessarily those of Rolls-Royce plc, Aerospace Group.

REFERENCES

1. Stillwagon LE, Larson RG. Leveling of thin films over uneven substrates during spin coating. *Physics of Fluids A* 1990; **2**(11):1937.
2. Peurrung LM, Graves DB. Film thickness profiles over topography in spin coating. *Journal of the Electrochemical Society* 1991; **138**(7):2115–2124.
3. Blyth MG, Pozrikidis C. Film flow down an inclined plane over a three-dimensional obstacle. *Physics of Fluids* 2006; **18**(5):052104–052114.
4. Hayes M, O'Brien G, Lammers JH. Greens function for steady flow over a small two-dimensional topography. *Physics of Fluids* 2000; **12**(11):2845–2858.
5. Gaskell PH, Jimack PK, Sellier M, Thompson HM, Wilson MCT. Gravity-driven flow of continuous thin liquid films on non-porous substrates with topography. *Journal of Fluid Mechanics* 2004; **509**(1):253–280.
6. Lee YC, Thompson HM, Gaskell PH. An efficient adaptive multigrid algorithm for predicting thin film flow on surfaces containing localized topographic features. *Computers and Fluids* 2007; **36**:838–855.
7. Sellier M. The flow of a thin liquid film past a cylinder. *COMSOL Users Conference 2006*, Frankfurt, 2006; 151–154.
8. Pozrikidis C, Thoroddsen ST. The deformation of a liquid film flowing down an inclined plane wall over a small particle arrested on the wall. *Physics of Fluids A* 1991; **3**(11):2546–2558.
9. Baxter SJ, Power H, Cliffe KA, Hibberd S. Three-dimensional thin film flow over and around an obstacle on an inclined plane. *Physics of Fluids* 2008; DOI: 10.1063/1.3082218.
10. Krishnasamy G, Rizzo FJ, Liu Y. Boundary integral equations for thin bodies. *International Journal for Numerical Methods in Engineering* 1994; **37**:107–121.
11. Lachat JC, Watson JO. Effective numerical treatment of boundary integrations: a formulation for three-dimensional elastostatics. *International Journal for Numerical Methods in Engineering* 1976; **10**(5):991–1005.
12. Hayami K. *Projection Transformation Method for Near Singular Surface Boundary Element Integrals*. Lecture Notes in Engineering. Springer: Berlin, 1992.
13. Mi Y, Aliabadi MH. Taylor expansion algorithm for integration of 3d near-hypersingular integrals. *Communications in Numerical Methods in Engineering* 1996; **12**(1):51.
14. Cutanda V, Juhl PM, Jacobsen F. On the modelling of narrow gaps using standard boundary element method. *Journal of the Acoustical Society of America* 2001; **109**(4):1296–1303.
15. La Rocca A, Hernandez Rosales A, Power H. Radial basis function hermite collocation approach for the solution of time dependent convection–diffusion problems. *Engineering Analysis with Boundary Elements* 2005; **29**(4):359–370.
16. Golberg MA, Chen CS. *Discrete Projection Methods for Integral Equations*. Computational Mechanics Publication: Southampton, 1997.